Change in Tropospheric Ozone in the Recent Decades and its Contribution to Global Total Ozone

Junhua Liu[1,2], Sarah A. Strode[1,2], Qing Liang[2], Luke D. Oman[2], Peter R. Colarco[2], Eric L. Fleming[3,2], Michael E. Manyin[3,2], Anne R. Douglass[2], Jerald R. Ziemke[1,2], Lok N. Lamsal[4,2], Can Li[5,2]

[1] Morgan State University, Baltimore, Maryland, USA

[2] NASA Goddard Space Flight Center, Greenbelt, Maryland, USA

[3] Science Systems and Applications, Inc., Lanham, MD, USA

[4] University of Maryland Baltimore County (UMBC), GESTAR II, Baltimore, Maryland, USA

[5] University of Maryland at College Park, Maryland, USA

Corresponding author: Junhua Liu (junhua.liu@nasa.gov)

Key points:

- Global total column ozone increased about 4 DU from 2005 to 2018 and about 60% of this increase due to tropospheric ozone.
- Tropospheric ozone increases depend primarily on increased regional emissions of ozone precursors, i.e. volatile organic compounds.
- The GEOSCCM model underestimates the observed tropospheric ozone increase, as a result of underestimated NO_2 emissions increase.

Abstract

Tropospheric ozone is a key chemically active trace gas and radiative forcer. Understanding its long-term changes is important to properly interpret observed changes in total column ozone and stratospheric ozone recovery. We investigate global and regional tropospheric ozone changes and their impact on total column ozone during 2005-2018 using satellite measurements and the NASA Goddard Earth Observing System Chemistry Climate Model (GEOSCCM). Global total ozone increased ~4 DU during 2005-2018 (+0.28±0.06 DU yr^{-1}) as inferred from Ozone Monitoring Instrument (OMI). Consistent with previous studies, the OMI/MLS (Microwave Limb Sounder) derived global tropospheric ozone increased 2.2 DU during this period, 60% of the global total column ozone increase. While GEOSCCM reproduces reasonably well the total column increase, it overestimates the stratospheric ozone increase and underestimates the tropospheric ozone increase.

We find that the tropospheric ozone increases are likely attributed to a growth of regional emissions of key ozone precursors, especially volatile organic compounds (VOCs) as reflected by the positive trends in formaldehyde (CH_2O). Although carbon monoxide (CO) has been decreasing everywhere around the globe, it has relatively small impact on the tropospheric ozone trend. Trends in nitrogen dioxide (NO_2) vary with regions, and these changes counteract or reinforce the positive effects of CH_2O on the tropospheric ozone increases. The model underestimates the observed tropospheric ozone increase, especially over the US and Europe, because of underestimated NO_2 emissions changes used in the model. The stratospheric ozone contribution increases during this period in the Northern Hemisphere and contributes to the tropospheric ozone increase.

1 Introduction

The ozone (O_3) layer in the stratosphere plays an important role in shielding the biosphere from dangerous solar ultraviolet (UV) radiation, shapes the temperature structure of the stratosphere, and consequently has a direct impact on the general circulation and tropospheric climate. The large ozone decline has been observed from the early satellite era (~1980) to the mid-1990s due to the increase of ozone-depleting substances (ODSs) [WMO 2014]. The concentrations of major ODSs have been declining with successful regulation of the Montreal Protocol since the late 1990s. Many studies based on observations and modeling have shown that latitudinally dependent ozone increases in the upper stratosphere from 2000 to 2016, as a result of declining ODSs and the enhancement of upper-stratospheric cooling associated with increases in greenhouse gases (GHG) [e.g., *Steinbrecht et al.*, 2017; *Ball et al.*, 2019; *Szelag et al.*, 2020]. The observed lower stratospheric ozone has shown a decrease from 2000 to 2016, but the trends are not significant due to large interannual dynamic variability [e.g., *Bourassa et al.*, 2014; *Sofieva et al.*, 2017; *Steinbrecht et al.*, 2017; *Ball et al.*, 2018]. Wargan et al [2018] concluded from chemistry transport model simulations that the observed decrease in lower stratospheric ozone was dominated by dynamically driven variability. Global and hemispheric means of total ozone derived from ground-based observations and merged products of satellite measurements have shown a few Dobson Units (DU) increase from 1997 to 2016, but have not generally shown a statistically significant positive trend [*Weber et al.*, 2018]. To assess the consistency between stratospheric profile trends and total column ozone trends, it is important to well quantify the changes in tropospheric ozone.

Tropospheric ozone is a short-lived trace gas that either originates naturally in the stratosphere [e.g., *Junge*, 1962; *Danielsen*, 1968; *Stohl et al.*, 2003] or is produced in situ by photochemical oxidation of non-methane volatile organic compounds (NMVOC), methane (CH_4) or carbon monoxide (CO) in the presence of nitrogen oxides (NO_X) [*Logan et al.*, 1981; Monk et al. 2009; 2015]. These precursors originate from anthropogenic fossil fuel and biofuel combustion, biomass burning emissions and from natural sources such as lightning and biogenic emissions. As a result of rapid growth in anthropogenic emissions due to industrialization, tropospheric ozone has increased significantly since the preindustrial era [e.g., *Marenco et al.*, 1994; *Volz and Kley*, 1988]. Anthropogenic ozone precursor emissions are continually changing in recent years. In Europe and North America, emissions decreased in the 1990s and 2000s as a result of regulation [*Cooper et al.*, 2010]. In East Asia and India, ozone precursor emissions have been increasing due to economic growth, with a regional shift of emissions from the Northern Hemisphere (NH) mid-high latitudes to lower latitudes [*Parrish et al.*, 2012]. Based on satellite observations of the Ozone Monitoring Instrument (OMI), Krotkov et al. [2016] shows that nitrogen dioxide (NO_2), a key ozone precursor, began to decrease over the north China Plain in 2011, with about a 50% reduction between 2012 and 2015. In addition, there was a complex heterogeneity of urban NO_2 changes around the world from 2005 to 2014 [*Duncan et al.*, 2016]. These changes in emissions appear to have impacted regional ozone trends, showing important variations from region to region over the past two decades. Despite the implementation of legislative standards to control ozone precursors emission worldwide, many previous studies from satellite data and model simulations show a tropospheric ozone increase during the past two decades [e.g., *Cooper et al.*, 2014; *P S Monks et al.*, 2015a; *Simon et al.*, 2015; *Sicard et al.*, 2016].

In this study, we carry out a model-data combined analysis using various satellite measurements and the NASA Goddard Earth Observing System Chemistry Climate Model (GEOSCCM) to quantify tropospheric ozone change and its contribution to total column ozone change. The current standard version of GEOSCCM uses the Global Modeling Initiative (GMI) stratosphere-troposphere full chemistry scheme [*Nielsen et al.*, 2017]. This provides a useful modeling tool to understand: (i) the change in tropospheric ozone, (ii) how the tropospheric ozone change contributes to the total column change, and (iii) how this information can be combined with satellite observations to assess the stratospheric ozone recovery. We also conduct a comprehensive analysis to compare GEOSCCM simulated tropospheric trace gases against satellite observations in the past two decades and evaluate the performance of GEOSCCM in reproducing the spatial and temporal variability of tropospheric ozone and its key photochemical precursors, i.e., NO_2, CH_2O and CO.

The simulation and various satellite datasets used in this study are briefly described in Section 2. Section 2 also describes the smoothing and simple linear regression (SLR) methods used in trend analysis. Section 3 presents the evaluation of tropospheric and total ozone and their trends analysis with a focus on the contribution of tropospheric ozone increase on changes in total ozone. This will allow us to look at the consistency between trends in tropospheric ozone, stratospheric ozone and total ozone. Analysis of regional changes in tropospheric ozone and its three key observed precursors (NO_2, CH_2O and CO) are presented and discussed in Section 4. Summary and final remarks are given in Section 5.

2 Model and observations

2.1 Model and simulation description

Model simulations presented in this work are conducted using the NASA GEOSCCM, which couples the Goddard Space Flight Center GEOS-5 Atmosphere-Ocean model [*Reinecker et al.*, 2008] with the GMI chemistry mechanism [*Duncan et al.*, 2007; *Strahan et al.*, 2007; *Nielsen et al.*, 2017] and the Goddard Chemistry Aerosol Radiation and Transport (GOCART) aerosol mechanism [*Chin et al.*, 2002; 2014; *Colarco et al.*, 2010]. GEOSCCM has been evaluated extensively for its performance in stratospheric ozone-related photochemistry and transport processes in various process-oriented model intercomparisons, including Stratosphere-troposphere Processes and their Role in Climate (SPARC) Chemistry Climate Model Validation (CCMVal), CCMVal-2, and the Chemistry-Climate Modeling Initiative (CCMI) [SPARC-CCMVal, *Eyring et al.*, 2010a; 2013; *Morgenstern et al.*, 2017; 2010].

The GMI mechanism includes 120 species and over 400 chemical reactions and reproduces well the observed atmospheric composition [e.g., *Liang et al.*, 2009; 2017b; *Strode et al.*, 2015b; 2019; *Liu et al.*, 2016; *Oman and Strahan*, 2016; *Prather et al.*, 2018;]. The GOCART aerosol module includes aerosols from anthropogenic, biomass burning, and natural sources (biogenic, volcanic, and wind-blown dust and sea salt) [*Chin et al.*, 2002; *Bian et al.*, 2014; 2017; 2019]. GEOSCCM uses a flux-form semi-Lagrangian dynamical core [*Lin*, 2004] and the Relaxed Arakawa Schubert (RAS) convective parameterization [*Moorthi and Suarez*, 1992]. The lightning parameterization follows an updated version of the scheme described by Allen et al [2010]. The regional lightning NOX emission, calculated online by coupling to the deep convective transport in the model, varies from year to year. The global total of NOX from lightning has small year-to-year differences, with values from 5.2 to 5.4 TgN/yr.

The simulation used in this study is a free-running hindcast simulation of 1960 – 2018 (CCMI Ref-D1). The hindcast simulation uses specified sea surface temperatures (SSTs) and sea ice concentrations (SICs), prescribed as monthly mean boundary conditions following the global HadISST1 data set provided by the UK Met Office Hadley Centre [*Rayner et al.*, 2003]. The Ref-D1 setup is organized by the CCMI in support of the 2022 World Meteorological Organization (WMO) Scientific Assessment of Ozone Depletion. Anthropogenic emissions are from the Community Emissions Data System [CEDS; *Hoesly et al.*, 2018] from the Coupled Model Intercomparison Project Phase 6 (CMIP6) for 1980 - 2014. For 2015 to 2017, emissions are from a middle-of-the-road scenario of Shared Socioeconomic Pathways targeting a forcing level of 4.5 Wm^{-2} (SSP2–4.5), from the CMIP6 ScenarioMIP experiment [*Gidden et al.*, 2019]. Biomass burning emissions are from the CMIP6 harmonized emission inventory as detailed in Van Marle et al. [2017] to the end of 2015. For 2016 and subsequent years, biomass burning emissions are calculated from the GFED4s database (https://globalfiredata.org/pages/data/#emissions). Anthropogenic and biomass burning emissions are represented by monthly gridded emissions including seasonal and interannual variability.

Global and regional means of annual anthropogenic emissions of NO_X, key VOCs, and CO in the model from 1960 to 2018 are presented in Figure 1. About 95% of global anthropogenic emissions occur in the NH and tropics, where the heavily populated and industrialized regions are located [*Masson-Delmotte et al.*, 2018]. The global NO_X, CO, and VOC emissions show similar variations,

with an increase between 1960 and 1990, followed by a weak decrease in VOC and CO or a relatively flat pattern in NO_X until 2000 - 2003, then followed by an abrupt increase until around 2011 and a decrease afterward. The tropical NO_X, VOC, and CO emissions in the model show a steady and significant increase from 1960 to 2015 and a slight decrease in the most recent years, driven by the emission variations over India, Indonesia, and Africa. Both NO_X and CO emissions in China increased steadily between 1970 and 2011; and decreased slightly after successful improvement of combustion efficiency and implementation of emissions control regulations in the most recent decade. The VOC emissions in China showed a similar increase as seen in NO_X and CO before 2011 but kept increasing in the most recent decade. The NO_X, VOC and CO emissions over United States (US) and Europe have been decreasing significantly since the 1970s. Overall, the negative trends over US and Europe after the 1970s was counteracted by the positive trends over China and India, resulting in little change in the northern hemispheric mean CO and VOC emissions between 1970 and 1990, and a negative trend after 1990.

The model includes a stratospheric ozone tracer ($StratO_3$). Using the $StratO_3$ tracer allows quantification of ozone of stratospheric origin in the troposphere at a given location and time. The $StratO_3$ is defined relative to a dynamically varying tropopause tracer (e90) [*Prather et al.*, 2011], which has been implemented in the GEOSCCM-GMI model. The e90 tracer is an artificial tracer emitted at the surface uniformly (100 ppb) with a 90-day e-folding lifetime. The $StratO_3$ tracer is set equal to ozone in the stratosphere and is removed in the troposphere with the loss frequency (chemistry and deposition) archived from daily output of its hindcast simulation. The simple O_X-HO_X cycle ($O(^1D) + H_2O \rightarrow 2\ OH$; $HO_2 + O_3 \rightarrow 2\ O_2 + OH$; $OH + O_3 \rightarrow HO_2 + O_2$) is applied to determine destruction of odd oxygen. $StratO_3$ does not track photochemical production of ozone in the troposphere; thus, no chemical production of ozone in the troposphere is added to the $StratO_3$ tracer. A similar approach has also been adopted in other CCMI participating models, e.g., the high resolution Geophysical Fluid Dynamics Laboratory Atmospheric Model 3 (GFDL AM3) [*Lin et al.*, 2012].

2.2 Satellite observations used for model evaluation

Accurate simulation of total ozone column change in global CCM requires adequate representation of stratospheric and tropospheric ozone. GEOSCCM stratospheric ozone has been extensively evaluated in previous studies [e.g., *Eyring et al.*, 2006; 2007; 2010a; 2010b; *Oman et al.*, 2010]. In this study, we aim to conduct a full assessment of model simulated tropospheric ozone and its key photochemical precursors, i.e., NO_2, CH_2O and CO using satellite observations from OMI/MLS onboard the Aura satellite and Measurement of Pollution in the Troposphere (MOPITT) onboard the Terra satellite. For model evaluation and comparison with satellite observations, we sample the GEOSCCM simulation of the corresponding trace gases that matches with satellite observations in time and space.

2.2.1 Ozone

Remote sensing observations of atmospheric ozone used in this study, including total column ozone (TOZ), tropospheric column ozone (TCO), and stratospheric column ozone (SCO), are from the NASA Aura OMI and MLS instruments. The TOZ is retrieved using the OMTO3 v8.5

algorithm [Bhartia, 2002] (http://disc.sci.gsfc.nasa.gov/Aura/data-holdings/OMI) that uses OMI retrieved centroid cloud pressure [*Vasilkov et al.*, 2008]. SCO is derived from MLS v4.2 ozone profiles [*Livesey et al.*, 2011] by integrating the MLS profiles from top of the atmosphere down to the tropopause. The tropopause pressure is determined from the WMO 2 K km^{-1} lapse-rate definition from NCEP re-analyses [*Randel et al.*, 2000]. TCO is derived by subtracting MLS SCO from OMI total column ozone each day at each grid point between 60°S and 60°N from 2004 to 2018 [*Ziemke et al.*, 2019], and is referred to as the OMI/MLS TCO hereafter. More details for the OMI/MLS TCO and SCO data are described in Ziemke et al. [2019].

2.2.2 Key ozone photochemical precursors: NO_2, CH_2O, CO

The various satellite observations used in this study include the tropospheric NO_2 column L3 product (v4.0) from the Aura OMI [*Lamsal et al.*, 2021], total CH_2O column product from the Aura OMI, and the total CO column and CO profiles L3 products (V8) from MOPITT on the NASA Terra satellite [*Deeter et al.*, 2019].

The retrieval algorithm for OMI NO_2 V4.0 is based on a conceptually new, geometry-dependent surface Lambertian equivalent reflectivity (GLER) data that are available on an OMI pixel basis. The GLER combined with consistently retrieved oxygen dimer (O_2-O_2) absorption-based cloud fractions and pressures provide high-quality data inputs to the new NO_2 retrieval scheme. The updates implemented in V4.0 yield higher (~10–40%) tropospheric NO_2 columns in polluted areas, with less-pronounced differences in background and low-column areas [*Lamsal et al.*, 2021]. The OMI NO_2 v4.0 shows significant improvement over polar region than the previous version, with enhanced data quality and extended coverage over snow/ice covered surface. To compare GEOSCCM simulations with the OMI tropospheric NO_2 column, we sample the model tropospheric NO_2 column at OMI/Aura overpass time (local 2pm). High quality NO_2 data with effective cloud fraction < 30% are used to create L3 tropospheric NO_2 column product. Here we use the observed and simulated NO_2 column changes to infer changes in NO_2 emission, which has been widely used in many previous studies [e.g., *Martin et al.*, 2003; *Streets et al.*, 2013; *Beirle et al.*, 2011; 2019; *Geng et al.*, 2017; *Shah et al.*, 2022] . The retrieved NO_2 slant columns are converted to vertical columns using air mass factors (AMFs) that accounts for the changes in observation sensitivity. The vertical sensitivity is not constant, it is a function of several factors including observation and solar geometries, cloud scenarios (cloud pressure and cloud fraction), surface reflectivity, and aerosols. The AMF also depends on the vertical distribution of NO_2 (a-priori NO_2 profile shapes). Over polluted regions, most of NO_2 is near the surface thereby enabling satellite observation of NO_2 despite somewhat reduced sensitivity. And the column is commonly viewed as a proxy for NO_x emissions over these regions. Over tropospheric background areas, where most NO_2 resides in the stratosphere, satellite tropospheric NO_2 retrievals are highly uncertain due to error in the separation of stratospheric and tropospheric components. However, if there are NO_2 plumes over satellite field of view, that information is detected in slant columns and consequently in vertical columns, although the estimated vertical columns may have slightly larger errors if proper a-priori information is not used in the retrievals.

We use the L3 gridded OMI total CH_2O column derived from OMI base on principal component analysis (PCA) retrieval algorithm for the period of October 2004 to December 2018. The PCA algorithm features enhanced sensitivity and reduced retrieval noise and artifacts. It also helps to mitigate some instrumental and calibration inconsistencies between different sensors, enabling the

production of long-term, consistent data records from multiple instruments such as OMI and SNPP/OMPS [*Li et al.*, 2017; *Zhang et al.*, 2017]. To reduce bias, the OMI retrievals are subject to a Pacific sector correction (PSC). The latitude dependent bias was first calculated over the remote East Pacific between the monthly mean OMI retrievals and a climatology of monthly CH_2O from multi-year simulations with the GMI chemical transport model. The same bias correction is then applied to all pixels within the same latitude band, regardless of their longitudes. The bias-corrected level 2 data are gridded to 0.25 degree by 0.25-degree resolution after excluding pixels with large cloud radiance fraction (> 0.5) or solar zenith angles (> 70 degree), and then averaged to produce monthly means used in this study. A detailed description of the PCA-based CH_2O retrieval algorithm can be found in Li et al. [2015].

The MOPITT V8 data incorporates an improved radiance bias correction method which has decreased the retrieval bias drift and geographically variable retrieval bias [*Deeter et al.*, 2019]. To compare GEOSCCM with MOPITT CO column and profile, we sampled the model profile at MOPITT overpass time (local 10 am), interpolated the model profiles to the MOPITT pressure grid (10 levels) and applied the MOPITT averaging kernel matrix, and integrated them to calculate the simulated CO column.

2.3 Methods for trend analysis

Trends presented in this study are reported as the linear rate of change (per year, yr^{-1}) over the period 2005 - 2018. The trends are calculated using a simple linear regression model on the gridded and low pass filtered monthly means. First, we calculate monthly mean values at each grid. We then follow the method as shown in Robertson and Dowling [2003] and apply a 13-month low pass Butterworth filter on these monthly means to eliminate the influence of high frequencies and the impact of autocorrelation. The Butterworth filter, well known in electrical engineering, is maximally flat in the passband and provides virtually no distortion of the low-frequency signal components [*Robertson and Dowling*, 2003]. Each trend value is accompanied by its 1.96 standard deviations ($1.96*\sigma$), which is commonly used in the construction of approximate 95% confidence interval [*Borradaile*, 2003] to determine whether a trend is statistically significant.

3 Tropospheric ozone change and its contribution to changes in total ozone

3.1 Evaluation of GEOSCCM RefD1 simulated ozone

Tropospheric Column Ozone (TCO). The OMI/MLS retrievals and GEOSCCM RefD1 simulation agree well with each other in the major features of global distribution of tropospheric ozone, showing ozone maxima over primary anthropogenic emission regions, i.e., East Asia, India, Middle East, Europe and the Eastern US (Figure 2, left panel). Both the model and observations show elevated ozone over the NH oceans and the south tropical Atlantic. The elevated ozone in the NH oceans reflects contributions of outflow of fossil fuel and biomass burning emissions from adjacent continents. The elevated ozone in the southern tropical Atlantic has been primarily attributed to lightning NO_x emissions with higher ozone production efficiency [e.g., *Jenkins and Ryu*, 2004; *Sauvage et al.*, 2007; *Liu et al.*, 2017b]. Liu et al [2017b] shows that downward transport of ozone from the stratosphere also contributes to the elevated ozone over the southern tropical Atlantic, with a significant influence in the upper troposphere. Both model and observations show ozone minima over the western Pacific warm pool, due to combined effects of

photochemical loss and inflow of clean tropical marine air with the development of deep convection [*Taupin et al.*, 1999; *Clain et al.*, 2009]. RefD1 TCO compares reasonably well with the OMI/MLS TCO over North and South America, tropical and mid-latitude oceans. Modeled ozone is biased high in most of Africa, the Middle East, and India, most likely due to high-biased NO_2 in these regions (Section 4.1). The model is biased low at high latitudes, especially in the Southern Hemisphere (SH). Ziemke et al. [2006] shows that the OMI/MLS TCO product has greater biases in wintertime high latitude due to the high solar zenith angles, where loss of ozone sensitivity is largest. Therefore, the model-observation difference at high latitudes might be caused by a latitude-dependent problem with OMI/MLS calibration.

Total column Ozone (TOZ). The GEOSCCM RefD1 simulation agrees well with the spatial and temporal variations of the OMI-retrieved TOZ (Figure 3, left panel). The model reproduces the strong latitudinal gradient in the observed total ozone, showing ozone maxima in the northern mid-high latitudes and ozone minima over the tropics. Compared to the observations, the model simulation features excessively high levels of ozone in the northern high latitudes but shows a slight low bias over the SH oceans. The observed global TOZ shows a significant increase with annual mean trends of ~ 0.28 DU/year (Figure 3, right panel). Expressed in absolute terms, such trends indicate about 4.0 DU and 1.4% increases in TOZ from 2005 to 2018. The model reproduces well the observed global total ozone increase. In the NH mid-high latitudes, although the positive trend is much stronger in the simulated total ozone than that in observations, neither of them are significant. In the tropics and the SH, both the model and observations show statistically significant increases in the total ozone.

3.2 Tropospheric ozone changes between 2005 and 2018

The observed tropospheric column ozone shows ubiquitous increases across most of the globe (Figure 4), with global mean TCO increases at a rate of ~0.16 DU yr^{-1} and a total increase of ~2.3 DU (7.2%) from 2005 to 2018 (Figure 2, right panel). The averaged TCO increases ranged from 1.5 to 3 DU during the past 14 years over many polluted regions with maxima over India, China and Indonesia. The strong positive trends of tropospheric ozone over India and China are primarily driven by their anthropogenic emissions increases [e.g., *Lal et al.*, 2012; *Cooper et al.*, 2014; *Sun et al.*, 2016; *Wang et al.*, 2017; *Lu et al.*, 2018; *Gaudel et al.*, 2020; *Baruah*, 2021]. The ozone increase over China during this period is slightly smaller than that over India. Several studies based on satellite observations have shown that NO_X emissions in China have been declining since 2012 due to stringent air pollution controls [e.g., *Duncan et al.*, 2016; *Krotkov et al.*, 2016; *Liu et al.*, 2017a], whereas in India NO_X emissions have continued increasing with a related deterioration in air quality [e.g., *Baruah*, 2021]. The strong positive trend of tropospheric column ozone over Indonesia is driven by intense fire activity in recent years as well as increasing pollution [*Rosanka et al.*, 2021]. The GEOSCCM RefD1 simulation captures well the sign and geographical features of the observed increases in tropospheric column ozone, but overall shows weaker trends in its global (~0.06 DU/yr, a total 0.8 DU increase for 2005-2018) and regional means. Over US, in contrast to the observed +2.0 DU increase, the model shows a weak negative trend, which is likely driven by the decreased anthropogenic emissions in the model. In the SH, the simulated TCO

315 shows a mostly positive trend, but not statistically significant. A more detailed discussion of
316 regional changes in tropospheric ozone as well as its key precursors is in section 4.

317 3.3 Contribution of TCO trends in total ozone

318 As shown in the Section 3.2, tropospheric ozone increased significantly from 2005 to 2018 almost
319 everywhere around the world. The resulting TCO change of a few DU can have a noticeable impact
320 on the total ozone changes. In this section, we assess the role of the tropospheric ozone trends on
321 total column changes and the relative importance with respect to the changes in stratospheric
322 column ozone using satellite observations and the GEOSCCM RefD1 simulation. Figure 5 shows
323 the temporal variations of simulated annual mean total column ozone with the tropospheric column
324 ozone stacked on top of the stratospheric column ozone from the RefD1 simulation between 1960
325 and 2018, superimposed on the annual mean of total column ozone from ground-based
326 observations and merged satellite observations [*Weber et al.*, 2018]. A five-year low pass filter has
327 been applied to the simulated ozone fields to highlight the long-term variations. The temporal
328 variations of simulated global total ozone in general agrees with that in observations from 1960 to
329 present. Both remained relatively stable prior to 1980, followed by a significant decrease between
330 1980 and 1997. After 1997, in addition to small year-to-year variations, total column ozone shows
331 a weak increase as a result of the successful regulation of ODS emissions under the Montreal
332 Protocol. The long-term change of global mean total ozone is consistent with changes in the
333 equivalent effective stratospheric chlorine (EESC) resulting from ODS changes (e.g., Weber et al.,
334 2018).

335 With satellite retrievals of global ozone, and the segregated tropospheric and stratospheric column
336 ozone information, available from the Aura OMI and MLS instruments from 2005 onward, it is
337 useful to combine these satellite remote sensing measurements with model simulations to
338 understand the relative contributions of changes in tropospheric and stratospheric ozone to the
339 change in the total column, especially over regions where tropospheric ozone shows strong
340 increases. Global total ozone increased ~4 DU (+0.3 DU/yr) from 2005 to 2018 as inferred from
341 the Aura OMI measurements (Figure 6). Consistent with previous studies, OMI/MLS TCO
342 suggests that global mean tropospheric ozone increased ~2.2 DU during this period, which
343 accounts for the majority (60%) of the increase in global total ozone. The observed global mean
344 stratospheric column ozone shows a slightly weaker but still significant positive trend during this
345 period, which coincides with the decline in ODSs. While GEOSCCM reproduces reasonably well
346 the total increase, it slightly underestimates the tropospheric ozone increase and overestimates the
347 stratospheric ozone increase. Ball et al. [2019] found that stratospheric column ozone, which is
348 dominated by lower-stratospheric ozone, decreased from 1998 to 2016, and analysis of merged
349 satellite datasets suggest a possible decrease in lower-stratospheric ozone over the past two
350 decades, although the uncertainty ranges are large [*Damadeo et al.*, 2018]. However, ozone trend
351 analysis is subject to large short-term dynamical variability [e.g., *Chipperfield et al.*, 2018],
352 natural variability [e.g., *Garfinkel et al.*, 2015; *Ball et al.*, 2020; *Iglesias-Suarez et al.*, 2021]. Since
353 the RefD1 simulation is a CCM simulation, which is not driven by specified dynamics, we do not
354 expect the GEOSCCM RefD1 simulation to reproduce the interannual variability of atmospheric
355 ozone. The overall agreement between model and observed SCO, TCO, and TOZ changes during

the Aura data period are reasonable, considering uncertainties due to the large dynamically-driven variabilities. GEOSCCM RefD1 simulation doesn't include chlorinated VSLS, but Chipperfield et al. [2018] suggest that the impact of very-short-lived halogenated substances (VSLS) on recent stratospheric ozone changes is small.

Figure 7 shows the global and hemispheric mean changes in ozone, including tropospheric, stratospheric, and total columns, from 2005 to 2018 derived from observations and the GEOSCCM RefD1 simulation. The observed positive trends in tropospheric ozone account for ~95% of the increase in the NH averaged total column ozone from 2005 to 2018. Over tropics, the total column ozone increased about 3.42 DU from 2005 to 2018, with 63% of the contribution from the tropospheric ozone increase and the remainder from the stratospheric ozone increase. In the SH, the increase in the observed mean stratospheric column ozone makes the dominant contribution (66%) to the total ozone changes. The high bias of simulated total ozone is largest in the NH mean, which is driven by the noticeable model overestimate in the stratosphere. In the NH, stratospheric column ozone trends derived from the Aura MLS measurements exhibit large spatial variations, showing decreases over the US and Europe, increases over China and India**,** and a much weaker negative change averaged over the NH ocean background (Figure S1). The counteraction of regional trend anomalies of observed stratospheric ozone leads to almost no trend in the NH averaged SCO from 2005 to 2018 (+0.12 DU, Figure 7). The model overestimates the observed trends in SCO over most regions in NH, which leads to the large model-overestimation of the observed NH mean trend (Figure. 7).

4 Effects of ozone precursors in tropospheric ozone trends

The analysis in the previous section revealed that tropospheric ozone plays an important role in total ozone trend. It is therefore desirable to further investigate the factors that drive tropospheric ozone changes. We selected four regions that have large anthropogenic emissions (US, Europe, India and China, which we define as "anthropogenic emissions regions"), and three regions with large biomass burning emissions (S. America, Africa and Indonesia, defined as "biomass burning regions") as shown in Figure 4. In addition, we include ocean regions between 30°N and 60°N (defined as "NH ocean background regions").

Ozone in the troposphere is produced by photochemical oxidation of CO, CH_4, and volatile organic compounds in the presence of NO_X [*Logan et al.*, 1981]. The efficiency with which atmospheric photochemistry produces ozone is a sensitive function of the VOC to NO_X ratio [e.g., *Sillman et al.*, 1990; *Tonnesen and Dennis*, 2000], and less sensitive to CO [e.g., *Logan et al.*, 1981]. NO_X acts as a catalyst in the photochemical production of ozone and plays a rate-determining role in ozone production in NO_X-limited regimes [e.g., *Duncan et al.*, 2010]. In NO_X-saturated (VOC-limited) regimes, which are in general the places with significant anthropogenic emissions, oxidation of CO, CH_4, and possibly other biogenic hydrocarbons leads to a net production of ozone and ozone becomes more sensitive to VOCs. CH_2O, a ubiquitous product of VOCs oxidation, is another key chemical related to VOCs and ozone formation [e.g., *Jin et al.*, 2017]. Although CH_2O is also directly emitted via biomass burning, fossil fuel combustion and natural gas flaring, oxidation of CH_4 and VOCs is the dominant production process of CH_2O [*Fortems-Cheiney et al.*,

2012]. Photolysis and reaction with OH destroy CH_2O with a characteristic lifetime of several hours during midday, implying that the CH_2O abundance primarily reflects recent CH_4 and VOC oxidation. CO plays a critical role in controlling the oxidizing capacity of the atmosphere through reaction with the primary tropospheric oxidant, the OH radial. Changes in CO directly affect tropospheric hydroxyl radicals, which affects the removal rate of dozens of man-made and anthropogenic trace gases.

In this section, we will focus on NO_2, CH_2O and CO, three key photochemical precursors of tropospheric ozone and conduct a full assessment of their model simulations using satellite observations from OMI/MLS onboard the Aura satellite and MOPITT onboard the Terra satellite. We will assess the regional trends of these precursors and their influence on tropospheric ozone changes.

4.1. Evaluations of ozone precursors (NO_2, CO and CH_2O) -global and climatological mean

4.1.1 NO_2

NO_2 is detectable from space and is currently retrieved with wide spatial coverage at a relatively high spatial resolution. The OMI/Aura NO_2 retrievals have a spatial resolution of 13 × 24 km^2 at nadir [*Levelt et al.*, 2006]. In general, the GEOSCCM RefD1 simulation reproduces the overall spatial distribution of observed tropospheric column NO_2 from Aura OMI. Both the model and observations show regional maxima of tropospheric column NO_2 (Ω_{NO2}) over North America, Europe, South Africa, and Asia, which are highly polluted areas with significant NO_X emissions (Figure 8). However, these polluted regions also exhibit significant model-observation biases. For example, the model is biased high over central and south Africa, northern Europe, northern India, and northeast and central China; and biased low in east China and east US. These discrepancies are present year-round and are likely attributed to biases in the CEDS anthropogenic emission inventory, especially in frontier and remote areas. In section 4.2 we discuss in detail these regional model vs. observation discrepancies.

The observed Ω_{NO2} shows significant positive trends (Figure 8, right panel). The absolute increases of Ω_{NO2} are similar among global and hemispheric Ω_{NO2} means (~5.6 x 10^{13} molec cm^{-2} from 2005 to 2018). However, the relative increase is largest over SH at a rate of 3.0% yr^{-1} and smallest over NH at a rate of ~0.3% yr^{-1}. The global mean increase is slightly less than 1% yr^{-1}. RefD1 does not show significant trends in global and southern hemispheric mean Ω_{NO2}. In the tropics, the relative increase of observed Ω_{NO2} is ~1.1% yr^{-1}, RefD1 shows a significant but much weaker positive trend (0.4% yr^{-1}). Although the RefD1 simulation does not reproduce the observed trends, it reproduces the phase of the observed seasonal cycle of Ω_{NO2}, showing strong model-observation correlations. Both simulated and observed Ω_{NO2} show winter maxima in each hemisphere, driven by an increased NO_2 lifetime, shallow mixing layer depth, and perhaps elevated anthropogenic emission sources during winter. However, the amplitude of the Ω_{NO2} seasonal cycle is overestimated in the GEOSCCM RefD1 simulation, especially for the global and northern hemispheric mean. Our regional analysis suggests that boreal regions have the largest discrepancies in seasonal cycle, which might be caused by the elevated errors in satellite retrievals over high latitude background areas [*Lamsal et al.*, 2021].

437 4.1.2 CH_2O

438 CH_2O is a ubiquitous product of almost all VOCs oxidation and has a short atmospheric lifetime
439 of a few hours against oxidation and photolysis. Therefore, its concentrations are widely used as a
440 reliable proxy of VOCs, which is a key precursor of tropospheric ozone. The RefD1 simulation
441 reproduces well the spatial distribution of total column CH_2O (Ω_{CH2O}) observed by Aura OMI
442 (Figure 9). Both show regional enhancements of CH_2O levels over the eastern US, South America,
443 central and south Africa, India, Indonesia, and China, which are the regions with high VOC
444 emissions from vegetation, fires, traffic, and industrial sources. Spatially, the largest discrepancies
445 are found over the eastern US and South America, where the model overestimates observed CH_2O
446 abundance by a factor of 2, primarily reflecting the overestimate in biogenic emissions. The RefD1
447 simulation did an excellent job in reproducing the temporal variations of observed CH_2O,
448 including trends, interannual variations, and seasonal cycles (Figure 9, right panel). Both observed
449 and simulated CH_2O show small but significant positive trends from 2005 to 2018, with the largest
450 increase in NH (obs: 0.6% yr^{-1}; model: 0.4%yr^{-1}), and the smallest but still significant increase in
451 the SH (obs: 0.2% yr^{-1}; model: 0.3% yr^{-1}). In the tropics, CH_2O increases significantly at a rate of
452 0.4% yr^{-1} from 2005 to 2018. Since CH_2O is a short-lived intermediate VOC oxidation product
453 and an important source of OH in the atmosphere, its atmospheric abundance is highly buffered
454 between its sources and sinks. As a result, this small trend in CH_2O abundance is not surprising.

455 4.1.3 CO

456

457 CO is another important ozone precursor. Its oxidation provides a source or sink for ozone,
458 depending on levels of nitrogen oxides. In general, the RefD1 simulation reproduces the global
459 variations of observed CO well, showing more polluted air and elevated CO in the NH than in the
460 SH, and higher CO concentrations in the tropical Atlantic than in the tropical Pacific (Figure 10).
461 Both observed and simulated total CO column show localized CO maxima over continents,
462 including areas of biomass burning source regions such as South America, southern Africa, and
463 areas dominated by anthropogenic emission such as eastern Asia and the eastern US. Elevated CO
464 exists downwind of these regions along the hemispheric subtropical jets and polar jets, indicating
465 strong longitudinal transport of polluted air within jet system. Clean air with low CO concentration
466 exists in the southern Pacific. CO reaches a minimum around 60°S in the Pacific, indicating the
467 combined effects of clean air and frequent occurrence of influx of low CO stratospheric air [e.g.,
468 *Robinson et al.*, 1984]. Over the Atlantic, CO maximum occurs over the tropics, driven in large
469 part by the outflow of southern hemispheric biomass burning [e.g., *Sinha et al.*, 2004]. Although
470 the model reproduces well the spatial variations of observed total CO from MOPPIT, several
471 regional discrepancies exist. The model shows persistent regional overestimates over Indonesia,
472 southern Africa, and southern China. Another dominant feature is that model underestimates the
473 observed CO over NH mid-high latitudes, which is a long-standing problem in many global
474 CTM/CCM simulations. It might be caused by too high OH and/or not enough emissions in the
475 model [e.g., *Shindell et al.*, 2006; *Duncan et al.*, 2007; *Monks et al.*, 2015b; *Strode et al.*, 2015a;
476 *Travis et al.*, 2020; *Keller et al.*, 2021]. The right panel shows the time series of global and

hemispheric mean of total column CO during the simulation period. The global observed total column CO decreases at a rate of 0.4% yr^{-1}, driven by the decreased anthropogenic emissions in the NH. The RefD1 shows a significant but much smaller trend in the NH total column CO.

4.2 Regional ozone changes and interpretation

In the following section we assess the regional trends of the key ozone precursors as well as the stratospheric ozone contribution to tropospheric ozone over the eight selected representative regions as defined above: four anthropogenic emissions regions (US, Europe, India and China), three biomass burning regions (S. America, Africa and Indonesia) and the NH ocean background regions. We discuss the effects of regional trends in key ozone precursors and trends in the stratospheric contribution on the regional trends in tropospheric ozone.

4.2.1 Anthropogenic emission regions

Figure 11 shows 13-month low pass filtered anomalies of regional and monthly mean observed and simulated tropospheric column ozone, its three key precursors (NO_2, CH_2O, CO) for four anthropogenic emission-dominated regions, the US, Europe, China, and India from 2005 to 2018. The bottom panel of Figure 11 shows the tropospheric column of the simulated $StratO_3$ tracer, which reflects temporal variations of the stratospheric ozone contribution in each region.

Over the US, the observed increasing trend of tropospheric ozone (0.14 ± 0.02 DU yr^{-1}) is likely primarily driven by the VOC increase as reflected by the observed increasing CH_2O abundances (Figure 11, 12). The OMI/MLS trend analysis suggests that the observed tropospheric ozone has increased by 5.7% during the past 14 years, with the maximum increase over the Midwest (Figure 12). While the RefD1 simulated TCO shows a weak decrease in its regional mean, the maximum decrease occurs over the southeast region with a slight increase over the western US. The OMI Ω_{NO2} shows a significant decrease from 2005 to 2009 and a much weaker decrease afterward. Overall, the OMI measurements suggest that Ω_{NO2} decreased 26.8% from 2005 to 2018 over the US. Instead of varying trends as shown in the observations, the RefD1 simulated Ω_{NO2} shows a steady and continuous decrease through the whole period. Spatially, the model reproduces well the negative trends of observed OMI Ω_{NO2} in urban US, with maximum decreases over the eastern US, and the San Francisco and Los Angeles megacities in California (Figure 12). Goldberg et al. (2021) showed that the bottom-up inventories including the CEDS inventory matched the combined top-down OMI NO_X estimates from 14 megacities in the US and Canada, in both trend and magnitude to within ±10%. The observed OMI Ω_{NO2} shows positive trends scattered in frontier and remote areas of the western and mid US, where the simulated Ω_{NO2} exhibits negative trends. The overall decrease in the simulated Ω_{NO2} is more than twice of that in the observation, and this decrease has offset the increase in TCO over the US due to increasing Ω_{CH2O} and stratospheric ozone contribution. The OMI observed Ω_{CH2O} over the US increased around 4% during this period, while RefD1 simulation fails to reproduce this positive trend in Ω_{CH2O}; instead, it shows an insignificant negative trend, which also contributes to the simulated negative trend in TCO over the US. The observed total column CO (Ω_{CO}) decreased about 8% from 2005 to 2018 over the US, while the model underestimates this negative trend and captures only 40% of the observed decrease.

The $StratO_3$ tracer simulation suggests that there is no significant increase in the stratospheric ozone contribution to tropospheric ozone over the US, during this period.

Over Europe, OMI/MLS year-to-year TCO variations change signs from negative to positive values but with an overall significant positive trend of 0.12 DU yr^{-1} during the 2005-2018 period. The RefD1 simulation underestimates the observed TCO increase, and only reproduced ~42% of the observed positive trends. Increases in simulated tropospheric ozone appear to be driven by: 1) VOCs increases as reflected by increased CH_2O abundances, and 2) increased stratospheric ozone contribution as indicated by the $StratO_3$ tracer simulation (Figure 11). Both the observations and simulation show comparable increases in Ω_{CH2O} and decreases in Ω_{CO}. While for Ω_{NO2}, the simulation averaged over Europe has a significant negative trend, which is five-time stronger than observed. The observed OMI Ω_{NO2} trends exhibit spatial heterogeneity (Figure 13), with positive trends in most regions of eastern Europe and negative trends in western, northern, and southern Europe, as well as Moscow, Russia. The counteraction of regional trend anomalies of observed Ω_{NO2} results in a weak but still significant negative trend averaged in the broader region of Europe. The model reproduces well the spatial variations and magnitudes of the observed Ω_{NO2} decreases, but fails to reproduce the observed increase in most regions of eastern Europe, showing strong negative trends almost everywhere in Europe. The much stronger negative trends of simulated Ω_{NO2} contributes to an underestimation in simulated TCO. The $StratO_3$ tracer in the model indicates a ~7% increase of stratospheric contribution to tropospheric ozone over Europe during this period. We found that although strong decreases are seen in Ω_{NO2} and Ω_{CO} over the US and Europe, the increased CH_2O concentration, which is likely caused by the increase in VOCs emission, leads to increases in the observed tropospheric ozone since 2005.The much stronger negative trends in simulated Ω_{NO2} over the rural areas in US and eastern Europe, which is likely caused by possibly exaggerated emission decrease in the model, contributes to the underestimates of TCO increases over these two regions.

Over China, both OMI/MLS and RefD1 simulation show a notable increase in tropospheric ozone, which appears to be driven by a combination of increased VOC, NO_2 and stratospheric ozone contribution (Figure 11). Unlike the continuous decrease of Ω_{NO2} seen over the US and Europe, OMI Ω_{NO2} shows a positive trend before 2011-12 followed by a decrease afterwards, resulting in an insignificant positive change during the 14-year period (2005-2018). In addition to the temporal variations, changes in OMI Ω_{NO2} exhibit strong spatial heterogeneity, with increases over rural area or small cities, and large decreases near megacities, including Beijing, Shanghai, and Pearl River Delta, which were likely drive by local emission control efforts (Figure 14). The RefD1 simulation reproduces the overall observed Ω_{NO2} temporal variations but shows a much weaker decrease after the 2011-12 maximum. Spatially, the model doesn't capture the observed Ω_{NO2} decrease over most megacities, except over Hong Kong. Both observed and simulated Ω_{CH2O} increased more than 10% during this period, indicating a significant increase of VOC over China and especially over eastern China. Both observed and simulated Ω_{CO} show a continuous decrease, primarily due to its decreasing anthropogenic emissions. The $StratO_3$ tracer in the model indicates that stratospheric contribution to the tropospheric ozone increased by 6% during 2005-2018.

India shows the largest TCO increases over the past 14 years, as a result of combined increases in VOCs, NO_2, and the stratospheric contribution (Figure 11). The OMI observations illustrate that both NO_2 and CH_2O show steady and significant increases of ~28% (Ω_{NO2}) and ~14% (Ω_{CH2O}) from 2005 to 2018. The RefD1 simulation produces comparable positive trends, with a slight overestimation of the observed positive trend in Ω_{NO2}, and a slight underestimation of the observed positive trend in Ω_{CH2O}. The positive trends in NO_2 and VOC likely reflect rapid industrialization, urbanization, traffic growth, and the limited effects of air quality policies on pollution sources in India during recent decades [e.g., *Vohra et al.*, 2021]. MOPITT Ω_{CO} decreased only 2% during the 14-year period (Figure 11), while the RefD1 simulation shows a stronger CO increase over India, which is likely driven by the increased Indian anthropogenic emissions used in the RefD1 simulation. The $StratO_3$ tracer simulation suggests a weak positive change (~1.5%) in stratospheric contribution to tropospheric ozone over India during this period.

4.2.2 Biomass burning emission regions

Over three biomass burning emission regions, increased tropospheric ozone appears to be related to increased VOC and NO_2, as well as increased stratospheric ozone (Figure 15). The OMI/MLS trend analysis suggests that the observed tropospheric ozone has increased significantly from 2005 to 2018 over all three biomass burning regions at a rate of 0.14 ± 0.02 DU yr^{-1} over South America, 0.15 ± 0.02 DU yr^{-1} over Africa and 0.21 ± 0.04 DU yr^{-1} over Indonesia. The RefD1 simulation underestimates the observed positive trends over these three regions and only produces about 30% of observed ozone increase over South America, and about 50% and 60% of observed ozone increase over Africa and Indonesia.

Over South America (Figure 15), OMI observations indicate that Ω_{NO2} increased by ~20% from 2005 to 2018, with Ω_{NO2} maxima in peak biomass burning years (2005, 2007, and 2010). The model captures the timing of the observed interannual Ω_{NO2} maxima but fails to reproduce the observed positive trend in Ω_{NO2}. Instead, the model simulated Ω_{NO2} decreased by 5.4% during this period, which contributes to the model's underestimation of observed TCO. The model in general reproduces well the OMI observed CH_2O changes, showing comparable increases from 2005 to 2018. Unlike the dominant positive trends in CH_2O, the observed CO from the MOPPIT instrument shows significant negative trends over the three selected regions. MOPITT observed CO decreased about 7% from 2005 to 2018 over South America. The model underestimates this observed negative trend, capturing only ~20% of the observed decrease. The $StratO_3$ tracer simulation suggests a weak but significant positive change in stratospheric contribution during this period.

Similar to South America, the model fails to reproduce the observed positive Ω_{NO2} trend over Africa, but with a much smaller discrepancy between observed and simulated Ω_{NO2} trends (Figure 15). The model reproduces well of the observed positive trend in OMI Ω_{CH2O}. MOPITT observations show a weaker negative trend (~-0.21% yr^{-1}) over Africa as compared to South America, while the model fails to reproduce the observed negative trends and shows an

insignificant positive trend. Compared to South America, the $StratO_3$ tracer simulation suggests a slightly stronger positive change in stratospheric contribution (5.6%) during this period.

Unlike South America and Africa, the model does a good job in simulating the observed Ω_{NO2} positive trend over Indonesia, where we find the smallest discrepancy between observed and simulated TCO trends among these three biomass-burning regions. Both observations and simulation show increased Ω_{NO2} (>1% yr^{-1}) and Ω_{CH2O} (> 0.5% yr^{-1}) over Indonesia, which contributes to the positive trend in TCO. MOPITT observed Ω_{CO} decreased at a rate of -0.4% yr^{-1}, while the model fails to reproduce the observed negative trends and shows a weak positive trend. Although the model does not reproduce the observed trend in CO, it reproduces the timing of the observed CO interannual maxima, including the 2015 maximum, the year of most severe fire activities and pollution over Indonesia since 2000s [e.g., *Field et al.*, 2016]. In addition to CO, CH_2O and NO_2 also reach to their maximum level in 2015, which contributes to the tropospheric ozone maximum during that year. The $StratO_3$ tracer simulation also suggests a weak but significant positive change in stratospheric contribution to tropospheric ozone during this period.

In summary, over these three biomass burning regions, the increase in TCO is mainly driven by the increases in its tropospheric photochemical precursors, i.e. VOCs and NO_2, and the stratospheric contribution. The model underestimates the observed TCO increases by 40-70%, which is mainly related to the underestimation of NO_2, as a result of underestimated NO_X emission changes used in the RefD1 simulation.

4.2.3 NH ocean background regions

Over the NH ocean background region, the observed and simulated positive TCO trend appears to be caused by the combined effects of significant increases in VOCs and stratospheric contribution (Figure 16). The OMI/MLS tropospheric ozone increased significantly from 2005 to 2018 at a rate of 0.17 ± 0.02 DU yr^{-1}. The RefD1 simulation underestimates the observed positive trends and only produces 40% of the observed TCO increase. Spatially, the model underestimates TCO almost everywhere over the NH ocean background region. The simulation shows a weak negative trend over the east coast of US and west coast of Europe, in contrast to the observed positive trends, which are dominated by much stronger negative trends of Ω_{NO2} in the model than those in the observations. The Ω_{NO2} bias is likely caused by downwind effects of the model biases in Ω_{NO2} trends from the rural US and eastern Europe as discussed in section 4.2.1. Similar to most selected NH regions, both observations and model show decreased CO and increased CH_2O during this period.

5 Conclusions

We have assessed the tropospheric column ozone change, globally and regionally, and quantified its contribution to the changes in total column ozone during the recent 14-year period (2005-2018) using a combination of various satellite measurements and the NASA GEOSCCM RefD1 simulation.

The observed global total ozone shows a small but significant increase, about +4 DU (+0.28 ± 0.06 DU yr^{-1}) from 2005 to 2018, as inferred by the OMI measurements. The observed global mean stratospheric column ozone shows a weak but still significant positive trend (+0.12 ± 0.04 DU yr-

1) during this period, which coincides with the decline in ODSs. Consistent with previous studies, the trend analysis of the OMI/MLS TCO suggests that the ozone trends in the troposphere are predominantly positive, and global mean tropospheric ozone increased ~2.8 DU (+0.16 ± 0.02 DU yr^{-1}) during this period, which contributes 60% of the global total ozone increase and plays a dominant role in the global total ozone variations. While GEOSCCM reproduces reasonably well the total column increase, it overly attributes most of this increase to the stratosphere ozone increase while underestimating the tropospheric ozone increase. Consider the large dynamic variability of ozone in the upper troposphere and stratosphere and the complexity in ozone trend analysis during a relatively short time period, these model biases are small.

In the troposphere, we have examined the global and regional trends of ozone in light of trends in key ozone precursors using satellite observations from OMI/MLS onboard the Aura satellite and MOPITT onboard the Terra satellite, as well as the RefD1 simulation. We find that the increases in ozone are likely attributed to a growth of regional emissions of key ozone precursors, especially VOCs. As a result of increasing VOCs emissions, atmospheric CH_2O abundances increase in most of the regions worldwide. While CO is co-emitted from combustion sources similar to VOCs, CO, unlike CH_2O and VOCs, has been decreasing everywhere around the globe, most likely reflecting decreasing emissions. The impact of CO on the tropospheric ozone trend is likely to be small. Unlike CH_2O and CO, NO_2 shows changes ranging from decreasing to increasing over different regions; there are relatively weak changes over three biomass burning regions, strong decreases over the US, Europe and NH ocean background region, strong increases over India, and a varied change over China. Overall, these changes in NO_2 counteract or reinforce the effects of positive trends in CH_2O on the tropospheric ozone increases.

Comparisons between the satellite observations and the RefD1 simulation of these ozone precursors also provide useful information on the accuracy of the emissions inventories used in the model. Our evaluation of the tropospheric column NO_2 simulations implies that the decrease of NO_2 emission from China after 2010 is likely underestimated, while the increase of NO_2 emissions from Indian is likely overestimated in the CEDS inventory (1980-2014) and SSP2-4.5 scenario (2015-2017). McDuffie et al. [2020] updated a new global anthropogenic emission inventory ($CEDS_{GBD\text{-}MAPS}$) based on the CEDS emission inventory. The new inventory extends the emission estimates from 2014 to 2017 and improves the overall agreement between CEDS and two widely used global bottom-up emission inventories: the EDGAR (Emissions Database for Global Atmospheric Research) [*Crippa et al.*, 2018], the ECLIPSE (Evaluating the Climate and Air Quality Impacts of Short-Lived Pollutants) [IIASA, 2015]. Their results suggest that over China and India, the updated $CEDS_{GBD\text{-}MAPS}$ NO_X emissions are generally lower than the CEDS inventory used in the model after the year 2010 because of the updated scaling inventory. Which are consistent with our comparison. Our NO_2 evaluation also suggests that NO_2 decreases from the rural US and eastern Europe in the model are likely inaccurate, which contributes to the underestimation of the observed TCO increase over and downwind of these regions. Here we attribute emissions errors as a main driver of errors in the trends of these ozone precursors, but it is important to note that other complicating factors also need to be considered, such as vertical distributions, missing sources other than emissions [*Shah et al.*, 2022].

Many studies [e.g., *Eichelberger and Hartmann*, 2005; *Garcia and Randel*, 2008; *Griffiths et al.*, 2021] have shown that in a changing climate the net stratosphere-to-troposphere mass transport will tend to increase due to a strengthened brewer-Dobson circulation. Meul et al [2018] suggested

that the global mean annual influx of stratospheric ozone into the troposphere is projected to increase by more than 50% between the years 2000 and 2100 under the RCP8.5 greenhouse gas scenario. Our model study suggests that in addition to the impacts of changes in ozone key precursors, the stratospheric ozone contribution to the troposphere in general shows a positive trend from 2005 to 2018 in the NH and contributes to the simulated tropospheric ozone increase. The positive trends in the stratospheric ozone contribution are likely caused by the combined effects of the increased stratospheric ozone concentrations in the model as well as possible enhanced stratosphere troposphere exchange. Given the observed and predicted net global decrease in emissions and the predicted increase in ozone STE, the relative importance of stratosphere–troposphere exchange of ozone versus in situ net chemical production for future tropospheric-ozone trends needs to be well assessed.

Acknowledgements:

This work was supported by NASA's Modeling, Analysis, and Prediction Program. Supercomputing resources for GEOSCCM were provided by the NASA High-End Computing (HEC) Program through the NASA Center for Climate Simulation (NCCS) at NASA Goddard Space Flight Center. GEOSCCM model description, configuration, input parameters and forcing datasets, and associated references are provided in section 2.1 of the main text. The authors thank Fei Liu for her helpful comments on top-down and bottom-up estimates of NO_2 emissions.

Open Research:

Fully sampled outputs of the GEOSCCM RefD1 simulation are available on the Center for Environmental Data Analysis (CEDA) archive as submitted for CCMI-2022 (https://data.ceda.ac.uk/badc/ccmi/data/post-cmip6/ccmi-2022/NASA-GSFC/GEOSCCM/refD1). Sub-sampled data at satellite overpass used in this study are archived on NASA National Center of Climate Simulation (NCCS) and available by request. All the satellite data are publicly available through NASA. The OMI/MLS tropospheric column ozone data and MLS stratospheric column ozone data [*Ziemke et al.*, 2019] can be downloaded from https://acd-ext.gsfc.nasa.gov/Data_services/cloud_slice/. The total ozone data (OMTO3 v8.5) [Bhartia, 2002] can be downloaded from NASA Goddard Earth Sciences Data and Information Service Center (GES DISC) (http://disc.sci.gsfc.nasa.gov/Aura/data-holdings/OMI). The OMI NO2 dataset [*Lamsal et al.*, 2021] can be downloaded from the GES DISC at https://disc.gsfc.nasa.gov/datasets/OMI_MINDS_NO2d_1/summary. The OMI total column CH_2O data [*Li et al.*, 2015] can be downloaded through the NASA Aura Validation Data Center (AVDC) site: https://avdc.gsfc.nasa.gov/index.php. The MOPITT carbon monoxide total column and profile data [*Deeter et al.*, 2019] can be downloaded from https://asdc.larc.nasa.gov/project/MOPITT/MOP03JM_8 (doi 10.5067/TERRA/MOPITT/MOP03JM_L3.008).

719 **Reference:**

720 Allen, D., K. Pickering, B. Duncan, and M. Damon (2010), Impact of lightning NO emissions on
721 North American photochemistry as determined using the Global Modeling Initiative (GMI)
722 model, *Journal of Geophysical Research-Atmospheres*, *115*, doi:10.1029/2010jd014062.
723 Ball, W. T., et al. (2018), Evidence for a continuous decline in lower stratospheric ozone offsetting
724 ozone layer recovery, *Atmospheric Chemistry and Physics*, *18*(2), 1379-1394,
725 doi:10.5194/acp-18-1379-2018.
726 Ball, W. T., J. Alsing, J. Staehelin, S. M. Davis, L. Froidevaux, and T. Peter (2019), Stratospheric
727 ozone trends for 1985-2018: sensitivity to recent large variability, *Atmospheric Chemistry
728 and Physics*, *19*(19), 12731-12748, doi:10.5194/acp-19-12731-2019.
729 Ball, W. T., G. Chiodo, M. Abalos, J. Alsing, and A. Stenke (2020), Inconsistencies between
730 chemistry-climate models and observed lower stratospheric ozone trends since 1998,
731 *Atmospheric Chemistry and Physics*, *20*(16), 9737-9752, doi:10.5194/acp-20-9737-2020.
732 Baruah, U. D. R., M. Scott Saikia, Anup Mili, Nitashree Sung, Kang Chand, Pritam
733 (2021), Spatio-temporal characterization of tropospheric ozone and its precursor pollutants
734 NO2 and HCHO over South Asia, edited, Science of The Total Environment, doi:ISSN
735 0048-9697.
736 Beirle, S., K. F. Boersma, U. Platt, M. G. Lawrence, and T. Wagner (2011), Megacity Emissions
737 and Lifetimes of Nitrogen Oxides Probed from Space, *Science*, *333*(6050), 1737-1739,
738 doi:10.1126/science.1207824.
739 Beirle, S., C. Borger, S. Dorner, A. Li, Z. K. Hu, F. Liu, Y. Wang, and T. Wagner (2019),
740 Pinpointing nitrogen oxide emissions from space, *Science Advances*, *5*(11),
741 doi:10.1126/sciadv.aax9800.
742 Bian, H. S., et al. (2017), Investigation of global particulate nitrate from the AeroCom phase III
743 experiment, *Atmospheric Chemistry and Physics*, *17*(21), 12911-12940, doi:10.5194/acp-
744 17-12911-2017.
745 Bian, H. S., et al. (2019), Observationally constrained analysis of sea salt aerosol in the marine
746 atmosphere, *Atmospheric Chemistry and Physics*, *19*(16), 10773-10785, doi:10.5194/acp-
747 19-10773-2019.
748 Borradaile, G. (2003), Theoretical Distributions: Binomial, Poisson and Normal Distributions., in
749 *Statistics of Earth Science Data*, edited, pp. pp. 61-75., Springer, Berlin, Heidelberg.
750 Bourassa, A. E., D. A. Degenstein, W. J. Randel, J. M. Zawodny, E. Kyrola, C. A. McLinden, C.
751 E. Sioris, and C. Z. Roth (2014), Trends in stratospheric ozone derived from merged SAGE
752 II and Odin-OSIRIS satellite observations, *Atmospheric Chemistry and Physics*, *14*(13),
753 6983-6994, doi:10.5194/acp-14-6983-2014.
754 Chin, M., et al. (2014), Multi-decadal aerosol variations from 1980 to 2009: a perspective from
755 observations and a global model, *Atmospheric Chemistry and Physics*, *14*(7), 3657-3690,
756 doi:10.5194/acp-14-3657-2014.
757 Chin, M., P. Ginoux, S. Kinne, O. Torres, B. N. Holben, B. N. Duncan, R. V. Martin, J. A. Logan,
758 A. Higurashi, and T. Nakajima (2002), Tropospheric aerosol optical thickness from the
759 GOCART model and comparisons with satellite and Sun photometer measurements, *Journal
760 of the Atmospheric Sciences*, *59*(3), 461-483, doi:10.1175/1520-
761 0469(2002)059<0461:taotft>2.0.co;2.
762 Chipperfield, M. P., S. Dhomse, R. Hossaini, W. H. Feng, M. L. Santee, M. Weber, J. P. Burrows,
763 J. D. Wild, D. Loyola, and M. Coldewey-Egbers (2018), On the Cause of Recent Variations

764 in Lower Stratospheric Ozone, *Geophysical Research Letters*, *45*(11), 5718-5726,
765 doi:10.1029/2018gl078071.
766 Clain, G., J. L. Baray, R. Delmas, R. Diab, J. L. de Bellevue, P. Keckhut, F. Posny, J. M. Metzger,
767 and J. P. Cammas (2009), Tropospheric ozone climatology at two Southern Hemisphere
768 tropical/subtropical sites, (Reunion Island and Irene, South Africa) from ozonesondes,
769 LIDAR, and in situ aircraft measurements, *Atmospheric Chemistry and Physics*, *9*(5), 1723-
770 1734.
771 Colarco, P., A. da Silva, M. Chin, and T. Diehl (2010), Online simulations of global aerosol
772 distributions in the NASA GEOS-4 model and comparisons to satellite and ground-based
773 aerosol optical depth, *Journal of Geophysical Research-Atmospheres*, *115*,
774 doi:10.1029/2009jd012820.
775 Cooper, O. R., et al. (2010), Increasing springtime ozone mixing ratios in the free troposphere over
776 western North America, *Nature*, *463*(7279), 344-348, doi:10.1038/nature08708.
777 Cooper, O. R., et al. (2014), Global distribution and trends of tropospheric ozone: An observation-
778 based review, *Elem. Sci. Anthropocene*, *2(1)*, doi:000029,
779 doi:10.12952/journal.elementa.000029.
780 Crippa, M., et al. (2018), Gridded emissions of air pollutants for the period 1970-2012 within
781 EDGAR v4.3.2, *Earth System Science Data*, *10*(4), 1987-2013, doi:10.5194/essd-10-1987-
782 2018.
783 Damadeo, R., I. Petropavlovskikh, S. Godin-Beekmann, D. Hubert, V. Sofieva, and B. Hassler
784 (2018), The Long-term Ozone Trends and Uncertainties in the Stratosphere (LOTUS)
785 SPARC activity: Lessons Learned, in: EGU General Assembly Conference Abstracts,
786 edited, Vienna, Austria, p. 9953, 2018.
787 Danielsen, E. F. (1968), Stratospheric-Tropospheric Exchange Based on Radioactivity, Ozone and
788 Potential Vorticity, *Journal of the Atmospheric Sciences*, *25*(3), 502-518, doi:10.1175/1520-
789 0469(1968)025<0502:stebor>2.0.co;2.
790 Deeter, M. N., D. P. Edwards, G. L. Francis, J. C. Gille, D. Mao, S. Martinez-Alonso, H. M.
791 Worden, D. Ziskin, and M. O. Andreae (2019), Radiance-based retrieval bias mitigation for
792 the MOPITT instrument: the version 8 product, *Atmospheric Measurement Techniques*,
793 *12*(8), 4561-4580, doi:10.5194/amt-12-4561-2019.
794 Duncan, B. N., L. N. Lamsal, A. M. Thompson, Y. Yoshida, Z. F. Lu, D. G. Streets, M. M. Hurwitz,
795 and K. E. Pickering (2016), A space-based, high-resolution view of notable changes in urban
796 NOx pollution around the world (2005-2014), *Journal of Geophysical Research-*
797 *Atmospheres*, *121*(2), 976-996, doi:10.1002/2015jd024121.
798 Duncan, B. N., J. A. Logan, I. Bey, I. A. Megretskaia, R. M. Yantosca, P. C. Novelli, N. B. Jones,
799 and C. P. Rinsland (2007), Global budget of CO, 1988-1997: Source estimates and validation
800 with a global model, *Journal of Geophysical Research-Atmospheres*, *112*(D22),
801 doi:10.1029/2007jd008459.
802 Duncan, B. N., et al. (2010), Application of OMI observations to a space-based indicator of NOx
803 and VOC controls on surface ozone formation, *Atmospheric Environment*, *44*(18), 2213-
804 2223, doi:10.1016/j.atmosenv.2010.03.010.
805 Eichelberger, S. J., and D. L. Hartmann (2005), Changes in the strength of the Brewer-Dobson
806 circulation in a simple AGCM, *Geophysical Research Letters*, *32*(15),
807 doi:10.1029/2005gl022924.

808 Eyring, V., et al. (2006), Assessment of temperature, trace species, and ozone in chemistry-climate
809 model simulations of the recent past, *Journal of Geophysical Research-Atmospheres*,
810 *111*(D22), 29, doi:10.1029/2006jd007327.
811 Eyring, V., et al. (2010a), Multi-model assessment of stratospheric ozone return dates and ozone
812 recovery in CCMVal-2 models, *Atmospheric Chemistry and Physics*, *10*(19), 9451-9472,
813 doi:10.5194/acp-10-9451-2010.
814 Eyring, V., et al. (2010b), Sensitivity of 21st century stratospheric ozone to greenhouse gas
815 scenarios, *Geophysical Research Letters*, *37*, 7, doi:10.1029/2010gl044443.
816 Eyring, V., et al. (2013), Overview of IGAC/SPARC Chemistry-Climate Model Initiative
817 (CCMI) Community Simulations in Support of Upcoming Ozone and Climate
818 Assessments, in *SPARC Newsletter 40*, edited, p. 18, WMO/SPARC, Zürich.
819 Eyring, V., et al. (2007), Multimodel projections of stratospheric ozone in the 21st century, *Journal*
820 *of Geophysical Research-Atmospheres*, *112*(D16), 24, doi:10.1029/2006jd008332.
821 Field, R. D., et al. (2016), Indonesian fire activity and smoke pollution in 2015 show persistent
822 nonlinear sensitivity to El Nino-induced drought, *Proceedings of the National Academy of*
823 *Sciences of the United States of America*, *113*(33), 9204-9209,
824 doi:10.1073/pnas.1524888113.
825 Fortems-Cheiney, A., F. Chevallier, I. Pison, P. Bousquet, M. Saunois, S. Szopa, C. Cressot, T. P.
826 Kurosu, K. Chance, and A. Fried (2012), The formaldehyde budget as seen by a global-scale
827 multi-constraint and multi-species inversion system, *Atmospheric Chemistry and Physics*,
828 *12*(15), 6699-6721, doi:10.5194/acp-12-6699-2012.
829 Garcia, R. R., and W. J. Randel (2008), Acceleration of the Brewer-Dobson circulation due to
830 increases in greenhouse gases, *Journal of the Atmospheric Sciences*, *65*(8), 2731-2739,
831 doi:10.1175/2008jas2712.1.
832 Garfinkel, C. I., D. W. Waugh, and L. M. Polvani (2015), Recent Hadley cell expansion: The role
833 of internal atmospheric variability in reconciling modeled and observed trends, *Geophysical*
834 *Research Letters*, *42*(24), 10824-10831, doi:10.1002/2015gl066942.
835 Gaudel, A., et al. (2020), Aircraft observations since the 1990s reveal increases of tropospheric
836 ozone at multiple locations across the Northern Hemisphere, *Science Advances*, *6*(34),
837 doi:10.1126/sciadv.aba8272.
838 Geng, G. N., Q. Zhang, R. V. Martin, J. T. Lin, H. Huo, B. Zheng, S. W. Wang, and K. B. He
839 (2017), Impact of spatial proxies on the representation of bottom-up emission inventories:
840 A satellite-based analysis, *Atmospheric Chemistry and Physics*, *17*(6), 4131-4145,
841 doi:10.5194/acp-17-4131-2017.
842 Gidden, M. J., et al. (2019), Global emissions pathways under different socioeconomic scenarios
843 for use in CMIP6: a dataset of harmonized emissions trajectories through the end of the
844 century, *Geoscientific Model Development*, *12*(4), 1443-1475, doi:10.5194/gmd-12-1443-
845 2019.
846 Griffiths, P. T., et al. (2021), Tropospheric ozone in CMIP6 simulations, *Atmospheric Chemistry*
847 *and Physics*, *21*(5), 4187-4218, doi:10.5194/acp-21-4187-2021.
848 Hoesly, R. M., et al. (2018), Historical (1750-2014) anthropogenic emissions of reactive gases and
849 aerosols from the Community Emissions Data System (CEDS), *Geoscientific Model*
850 *Development*, *11*(1), 369-408, doi:10.5194/gmd-11-369-2018.

Iglesias-Suarez, F., et al. (2021), Tropical Stratospheric Circulation and Ozone Coupled to Pacific Multi-Decadal Variability, *Geophysical Research Letters*, *48*(11), doi:10.1029/2020gl092162.

IIASA (2015), ECLIPSE v5a, edited, p. available at: https://www.iiasa.ac.at/web/home/research/researchPrograms/air/ECLIPSEv5a.html

Jenkins, G. S., and J. H. Ryu (2004), Space-borne observations link the tropical atlantic ozone maximum and paradox to lightning, *Atmospheric Chemistry and Physics*, *4*, 361-375.

Jin, X. M., et al. (2017), Evaluating a Space-Based Indicator of Surface Ozone-NOx-VOC Sensitivity Over Midlatitude Source Regions and Application to Decadal Trends, *Journal of Geophysical Research-Atmospheres*, *122*(19), 10231-10253, doi:10.1002/2017jd026720.

Junge, C. E. (1962), GLOBAL OZONE BUDGET AND EXCHANGE BETWEEN STRATOSPHERE AND TROPOSPHERE, *Tellus*, *14*(4), 363-377, doi:10.3402/tellusa.v14i4.9563.

Keller, C. A., et al. (2021), Description of the NASA GEOS Composition Forecast Modeling System GEOS-CF v1.0, *Journal of Advances in Modeling Earth Systems*, *13*(4), doi:10.1029/2020ms002413.

Krotkov, N. A., et al. (2016), Aura OMI observations of regional SO2 and NO2 pollution changes from 2005 to 2015, *Atmospheric Chemistry and Physics*, *16*(7), 4605-4629, doi:10.5194/acp-16-4605-2016.

Lal, D. M., S. D. Ghude, S. D. Patil, S. H. Kulkarni, C. Jena, S. Tiwari, and M. K. Srivastava (2012), Tropospheric ozone and aerosol long-term trends over the Indo-Gangetic Plain (IGP), India, *Atmospheric Research*, *116*, 82-92, doi:10.1016/j.atmosres.2012.02.014.

Lamsal, L. N., et al. (2021), Ozone Monitoring Instrument (OMI) Aura nitrogen dioxide standard product version 4.0 with improved surface and cloud treatments, *Atmospheric Measurement Techniques*, *14*(1), 455-479, doi:10.5194/amt-14-455-2021.

Levelt, P. F., G. H. J. Van den Oord, M. R. Dobber, A. Malkki, H. Visser, J. de Vries, P. Stammes, J. O. V. Lundell, and H. Saari (2006), The Ozone Monitoring Instrument, *Ieee Transactions on Geoscience and Remote Sensing*, *44*(5), 1093-1101, doi:10.1109/tgrs.2006.872333.

Li, C., J. Joiner, N. A. Krotkov, and L. Dunlap (2015), A new method for global retrievals of HCHO total columns from the Suomi National Polar-orbiting Partnership Ozone Mapping and Profiler Suite, *Geophysical Research Letters*, *42*(7), 2515-2522, doi:10.1002/2015gl063204.

Li, C., et al. (2017), India Is Overtaking China as the World's Largest Emitter of Anthropogenic Sulfur Dioxide, *Scientific Reports*, *7*, doi:10.1038/s41598-017-14639-8.

Liang, Q., A. R. Douglass, B. N. Duncan, R. S. Stolarski, and J. C. Witte (2009), The governing processes and timescales of stratosphere-to-troposphere transport and its contribution to ozone in the Arctic troposphere, *Atmospheric Chemistry and Physics*, *9*(9), 3011-3025, doi:10.5194/acp-9-3011-2009.

Lin, M., A. M. Fiore, O. R. Cooper, L. W. Horowitz, A. O. Langford, H. Levy, II, B. J. Johnson, V. Naik, S. J. Oltmans, and C. J. Senff (2012), Springtime high surface ozone events over the western United States: Quantifying the role of stratospheric intrusions, *Journal of Geophysical Research-Atmospheres*, *117*, doi:10.1029/2012jd018151.

Lin, S. J. (2004), A "vertically Lagrangian" finite-volume dynamical core for global models, *Monthly Weather Review*, *132*(10), 2293-2307, doi:10.1175/1520-0493(2004)132<2293:avlfdc>2.0.co;2.

Liu, F., S. Beirle, Q. Zhang, R. J. van der A, B. Zheng, D. Tong, and K. B. He (2017a), NOx emission trends over Chinese cities estimated from OMI observations during 2005 to 2015, *Atmospheric Chemistry and Physics*, *17*(15), 9261-9275, doi:10.5194/acp-17-9261-2017.

Liu, J., J. M. Rodriguez, S. D. Steenrod, A. R. Douglass, J. A. Logan, M. A. Olsen, K. Wargan, and J. R. Ziemke (2017b), Causes of interannual variability over the southern hemispheric tropospheric ozone maximum, *Atmospheric Chemistry and Physics*, *17*(5), 3279-3299, doi:10.5194/acp-17-3279-2017.

Liu, J., J. M. Rodriguez, A. M. Thompson, J. A. Logan, A. R. Douglass, M. A. Olsen, S. D. Steenrod, and F. Posny (2016), Origins of tropospheric ozone interannual variation over Reunion: A model investigation, *Journal of Geophysical Research-Atmospheres*, *121*(1), 521-537, doi:10.1002/2015jd023981.

Livesey, N. J., et al. (2011), EOS MLS Version 3.3 Level 2 data quality and description document*Rep.*

Logan, J. A., M. J. Prather, S. C. Wofsy, and M. B. McElroy (1981), TROPOSPHERIC CHEMISTRY - A GLOBAL PERSPECTIVE, *Journal of Geophysical Research-Oceans and Atmospheres*, *86*(NC8), 7210-7254, doi:10.1029/JC086iC08p07210.

Lu, X., L. Zhang, X. Liu, M. Gao, Y. Zhao, and J. Shao (2018), Lower tropospheric ozone over India and its linkage to the South Asian monsoon, *Atmospheric Chemistry and Physics*, *18*(5), 3101-3118, doi:10.5194/acp-18-3101-2018.

Marenco, A., H. Gouget, P. Nedelec, J. P. Pages, and F. Karcher (1994), EVIDENCE OF A LONG-TERM INCREASE IN TROPOSPHERIC OZONE FROM PIC DU MIDI DATA SERIES - CONSEQUENCES - POSITIVE RADIATIVE FORCING, *Journal of Geophysical Research-Atmospheres*, *99*(D8), 16617-16632, doi:10.1029/94jd00021.

Martin, R. V., D. J. Jacob, K. Chance, T. P. Kurosu, P. I. Palmer, and M. J. Evans (2003), Global inventory of nitrogen oxide emissions constrained by space-based observations of NO2 columns, *Journal of Geophysical Research-Atmospheres*, *108*(D17), doi:10.1029/2003jd003453.

Masson-Delmotte, V., et al. (2018), Global warming of 1.5 C, in *An IPCC Special Report on the impacts of global warming* edited.

McDuffie, E. E., S. J. Smith, P. O'Rourke, K. Tibrewal, C. Venkataraman, E. A. Marais, B. Zheng, M. Crippa, M. Brauer, and R. V. Martin (2020), A global anthropogenic emission inventory of atmospheric pollutants from sector- and fuel-specific sources (1970-2017): an application of the Community Emissions Data System (CEDS), *Earth System Science Data*, *12*(4), 3413-3442, doi:10.5194/essd-12-3413-2020.

Meul, S., U. Langematz, P. Kroger, S. Oberlander-Hayn, and P. Jockel (2018), Future changes in the stratosphere-to-troposphere ozone mass flux and the contribution from climate change and ozone recovery, *Atmospheric Chemistry and Physics*, *18*(10), 7721-7738, doi:10.5194/acp-18-7721-2018.

Monks, P. S., et al. (2015a), Tropospheric ozone and its precursors from the urban to the global scale from air quality to short-lived climate forcer, *Atmospheric Chemistry and Physics*, *15*(15), 8889-8973, doi:10.5194/acp-15-8889-2015.

Monks, P. S., et al. (2009), Atmospheric composition change - global and regional air quality, *Atmospheric Environment*, *43*(33), 5268-5350, doi:10.1016/j.atmosenv.2009.08.021.

939 Monks, S. A., et al. (2015b), Multi-model study of chemical and physical controls on transport of
940 anthropogenic and biomass burning pollution to the Arctic, *Atmospheric Chemistry and*
941 *Physics*, *15*(6), 3575-3603, doi:10.5194/acp-15-3575-2015.
942 Moorthi, S., and M. J. Suarez (1992), RELAXED ARAKAWA-SCHUBERT - A
943 PARAMETERIZATION OF MOIST CONVECTION FOR GENERAL-CIRCULATION
944 MODELS, *Monthly Weather Review*, *120*(6), 978-1002, doi:10.1175/1520-
945 0493(1992)120<0978:rasapo>2.0.co;2.
946 Morgenstern, O., et al. (2017), Review of the global models used within phase 1 of the Chemistry-
947 Climate Model Initiative (CCMI), *Geoscientific Model Development*, *10*(2), 639-671,
948 doi:10.5194/gmd-10-639-2017.
949 Nielsen, J. E., et al. (2017), Chemical Mechanisms and Their Applications in the Goddard Earth
950 Observing System (GEOS) Earth System Model, *Journal of Advances in Modeling Earth*
951 *Systems*, *9*(8), 3019-3044, doi:10.1002/2017ms001011.
952 Oman, L. D., et al. (2010), Multimodel assessment of the factors driving stratospheric ozone
953 evolution over the 21st century, *Journal of Geophysical Research-Atmospheres*, *115*, 21,
954 doi:10.1029/2010jd014362.
955 Oman, L. D., and S. E. Strahan (2016), Chemistry Simulations using MERRA-2 Reanalysis with
956 the GMI CTM and Replay in Support of the Atmospheric Composition Community, edited,
957 EOS Aura Science Team Meeting 2016,.
958 P., B. (2002), OMI algorithm theoretical basis document, volume II, OMI ozone products. *Rep.*,
959 NASA-OMI, Washington, ATBD-OMI-02, version 2.
960 Parrish, D. D., et al. (2012), Long-term changes in lower tropospheric baseline ozone
961 concentrations at northern mid-latitudes, *Atmospheric Chemistry and Physics*, *12*(23),
962 11485-11504, doi:10.5194/acp-12-11485-2012.
963 Prather, M. J., C. M. Flynn, X. Zhu, S. D. Steenrod, S. A. Strode, A. M. Fiore, G. Correa, L. T.
964 Murray, and J. F. Lamarque (2018), How well can global chemistry models calculate the
965 reactivity of short-lived greenhouse gases in the remote troposphere, knowing the chemical
966 composition, *Atmospheric Measurement Techniques*, *11*(5), 2653-2668, doi:10.5194/amt-
967 11-2653-2018.
968 Prather, M. J., X. Zhu, Q. Tang, J. Hsu, and J. L. Neu (2011), An atmospheric chemist in search
969 of the tropopause, *Journal of Geophysical Research-Atmospheres*, *116*,
970 doi:10.1029/2010jd014939.
971 Randel, W. J., F. Wu, and D. J. Gaffen (2000), Interannual variability of the tropical tropopause
972 derived from radiosonde data and NCEP reanalyses, *Journal of Geophysical Research-*
973 *Atmospheres*, *105*(D12), 15509-15523, doi:10.1029/2000jd900155.
974 Rayner, N. A., D. E. Parker, E. B. Horton, C. K. Folland, L. V. Alexander, D. P. Rowell, E. C.
975 Kent, and A. Kaplan (2003), Global analyses of sea surface temperature, sea ice, and night
976 marine air temperature since the late nineteenth century, *Journal of Geophysical Research-*
977 *Atmospheres*, *108*(D14), doi:10.1029/2002jd002670.
978 Reinecker, M. M., et al. (2008), The GEOS-5 Data Assimilation System-Documentation of
979 Versions 5.0. 1, 5.1. 0, and 5.2. 0*Rep.*, NASA, Greenbelt, MD.
980 Robertson, D. G. E., and J. J. Dowling (2003), Design and responses of Butterworth and critically
981 damped digital filters, *Journal of Electromyography and Kinesiology*, *13*(6), 569-573,
982 doi:10.1016/s1050-6411(03)00080-4.

983 Robinson, E., D. Clark, and W. Seiler (1984), THE LATITUDINAL DISTRIBUTION OF
984 CARBON-MONOXIDE ACROSS THE PACIFIC FROM CALIFORNIA TO
985 ANTARCTICA, *Journal of Atmospheric Chemistry*, *1*(2), 137-149,
986 doi:10.1007/bf00053836.
987 Rosanka, S., B. Franco, L. Clarisse, P. F. Coheur, A. Pozzer, A. Wahner, and D. Taraborrelli
988 (2021), The impact of organic pollutants from Indonesian peatland fires on the tropospheric
989 and lower stratospheric composition, *Atmospheric Chemistry and Physics*, *21*(14), 11257-
990 11288, doi:10.5194/acp-21-11257-2021.
991 Sauvage, B., R. V. Martin, A. van Donkelaar, and J. R. Ziemke (2007), Quantification of the
992 factors controlling tropical tropospheric ozone and the South Atlantic maximum, *Journal of*
993 *Geophysical Research-Atmospheres*, *112*(D11), doi:10.1029/2006jd008008.
994 Shah, V., et al. (2022), Nitrogen oxides in the free troposphere: Implications for tropospheric
995 oxidants and the interpretation of satellite NO 2 measurements, *EGUsphere*,
996 doi:https://doi.org/10.5194/egusphere-2022-656.
997 Shindell, D. T., G. Faluvegi, N. Unger, E. Aguilar, G. A. Schmidt, D. M. Koch, S. E. Bauer, and
998 R. L. Miller (2006), Simulations of preindustrial, present-day, and 2100 conditions in the
999 NASA GISS composition and climate model G-PUCCINI, *Atmospheric Chemistry and*
1000 *Physics*, *6*, 4427-4459, doi:10.5194/acp-6-4427-2006.
1001 Sicard, P., R. Serra, and P. Rossello (2016), Spatiotemporal trends in ground-level ozone
1002 concentrations and metrics in France over the time period 1999-2012, *Environmental*
1003 *Research*, *149*, 122-144, doi:10.1016/j.envres.2016.05.014.
1004 Sillman, S., J. A. Logan, and S. C. Wofsy (1990), THE SENSITIVITY OF OZONE TO
1005 NITROGEN-OXIDES AND HYDROCARBONS IN REGIONAL OZONE EPISODES,
1006 *Journal of Geophysical Research-Atmospheres*, *95*(D2), 1837-1851,
1007 doi:10.1029/JD095iD02p01837.
1008 Simon, H., A. Reff, B. Wells, J. Xing, and N. Frank (2015), Ozone Trends Across the United States
1009 over a Period of Decreasing NOx and VOC Emissions, *Environmental Science &*
1010 *Technology*, *49*(1), 186-195, doi:10.1021/es504514z.
1011 Sinha, P., L. Jaegle, P. V. Hobbs, and Q. Liang (2004), Transport of biomass burning emissions
1012 from southern Africa, *Journal of Geophysical Research-Atmospheres*, *109*(D20),
1013 doi:10.1029/2004jd005044.
1014 Sofieva, V. F., et al. (2017), Merged SAGE II, Ozone_cci and OMPS ozone profile dataset and
1015 evaluation of ozone trends in the stratosphere, *Atmospheric Chemistry and Physics*, *17*(20),
1016 12533-12552, doi:10.5194/acp-17-12533-2017.
1017 SPARC-CCMVal (2010), SPARC Report on the Evaluation of Chemistry-Climate Models, edited
1018 by *SPARC Rep. 5Rep.*, Univ. of Toronto, Toronto, Ont., Canada. (Available at
1019 http://www.atmosp.physics.utoronto.ca/SPARC.).
1020 Steinbrecht, W., et al. (2017), An update on ozone profile trends for the period 2000 to 2016,
1021 *Atmospheric Chemistry and Physics*, *17*(17), 10675-10690, doi:10.5194/acp-17-10675-2017.
1022 Stohl, A., et al. (2003), Stratosphere-troposphere exchange: A review, and what we have learned
1023 from STACCATO, *Journal of Geophysical Research-Atmospheres*, *108*(D12),
1024 doi:10.1029/2002jd002490.
1025 Strahan, S. E., B. N. Duncan, and P. Hoor (2007), Observationally derived transport diagnostics
1026 for the lowermost stratosphere and their application to the GMI chemistry and transport
1027 model, *Atmospheric Chemistry and Physics*, *7*(9), 2435-2445.

1028 Streets, D. G., et al. (2013), Emissions estimation from satellite retrievals: A review of current
1029 capability, *Atmospheric Environment*, *77*, 1011-1042, doi:10.1016/j.atmosenv.2013.05.051.
1030 Strode, S. A., B. N. Duncan, E. A. Yegorova, J. Kouatchou, J. R. Ziemke, and A. R. Douglass
1031 (2015a), Implications of carbon monoxide bias for methane lifetime and atmospheric
1032 composition in chemistry climate models, *Atmospheric Chemistry and Physics*, *15*(20),
1033 11789-11805, doi:10.5194/acp-15-11789-2015.
1034 Strode, S. A., J. M. Rodriguez, J. A. Logan, O. R. Cooper, J. C. Witte, L. N. Lamsal, M. Damon,
1035 B. Van Aartsen, S. D. Steenrod, and S. E. Strahan (2015b), Trends and variability in surface
1036 ozone over the United States, *Journal of Geophysical Research-Atmospheres*, *120*(17),
1037 9020-9042, doi:10.1002/2014jd022784.
1038 Strode, S. A., J. R. Ziemke, L. D. Oman, L. N. Lamsal, M. A. Olsen, and J. H. Liu (2019), Global
1039 changes in the diurnal cycle of surface ozone, *Atmospheric Environment*, *199*, 323-333,
1040 doi:10.1016/j.atmosenv.2018.11.028.
1041 Sun, L., et al. (2016), Significant increase of summertime ozone at Mount Tai in Central Eastern
1042 China, *Atmospheric Chemistry and Physics*, *16*(16), 10637-10650, doi:10.5194/acp-16-
1043 10637-2016.
1044 Szelag, M. E., V. F. Sofieva, D. Degenstein, C. Roth, S. Davis, and L. Froidevaux (2020), Seasonal
1045 stratospheric ozone trends over 2000-2018 derived from several merged data sets,
1046 *Atmospheric Chemistry and Physics*, *20*(11), 7035-7047, doi:10.5194/acp-20-7035-2020.
1047 Taupin, F. G., M. Bessafi, S. Baldy, and P. J. Bremaud (1999), Tropospheric ozone above the
1048 southwestern Indian Ocean is strongly linked to dynamical conditions prevailing in the
1049 tropics, *Journal of Geophysical Research-Atmospheres*, *104*(D7), 8057-8066,
1050 doi:10.1029/98jd02456.
1051 Tonnesen, G. S., and R. L. Dennis (2000), Analysis of radical propagation efficiency to assess
1052 ozone sensitivity to hydrocarbons and NOx 2. Long-lived species as indicators of ozone
1053 concentration sensitivity, *Journal of Geophysical Research-Atmospheres*, *105*(D7), 9227-
1054 9241, doi:10.1029/1999jd900372.
1055 Travis, K. R., et al. (2020), Constraining remote oxidation capacity with ATom observations,
1056 *Atmospheric Chemistry and Physics*, *20*(13), 7753-7781, doi:10.5194/acp-20-7753-2020.
1057 van Marle, M. J. E., et al. (2017), Historic global biomass burning emissions for CMIP6
1058 (BB4CMIP) based on merging satellite observations with proxies and fire models (1750-
1059 2015), *Geoscientific Model Development*, *10*(9), 3329-3357, doi:10.5194/gmd-10-3329-
1060 2017.
1061 Vasilkov, A., J. Joiner, R. Spurr, P. K. Bhartia, P. Levelt, and G. Stephens (2008), Evaluation of
1062 the OMI cloud pressures derived from rotational Raman scattering by comparisons with
1063 other satellite data and radiative transfer simulations, *Journal of Geophysical Research-*
1064 *Atmospheres*, *113*(D15), 12, doi:10.1029/2007jd008689.
1065 Vohra, K., et al. (2021), Long-term trends in air quality in major cities in the UK and India: a view
1066 from space, *Atmospheric Chemistry and Physics*, *21*(8), 6275-6296, doi:10.5194/acp-21-
1067 6275-2021.
1068 Volz, A., and D. Kley (1988), EVALUATION OF THE MONTSOURIS SERIES OF OZONE
1069 MEASUREMENTS MADE IN THE 19TH-CENTURY, *Nature*, *332*(6161), 240-242,
1070 doi:10.1038/332240a0.
1071 Wang, T., L. K. Xue, P. Brimblecombe, Y. F. Lam, L. Li, and L. Zhang (2017), Ozone pollution
1072 in China: A review of concentrations, meteorological influences, chemical precursors, and

effects, *Science of the Total Environment*, *575*, 1582-1596, doi:10.1016/j.scitotenv.2016.10.081.

Wargan, K., C. Orbe, S. Pawson, J. R. Ziemke, L. D. Oman, M. A. Olsen, L. Coy, and K. E. Knowland (2018), Recent Decline in Extratropical Lower Stratospheric Ozone Attributed to Circulation Changes, *Geophysical Research Letters*, *45*(10), 5166-5176, doi:10.1029/2018gl077406.

Weber, M., M. Coldewey-Egbers, V. E. Fioletov, S. M. Frith, J. D. Wild, J. P. Burrows, C. S. Long, and D. Loyola (2018), Total ozone trends from 1979 to 2016 derived from five merged observational datasets - the emergence into ozone recovery, *Atmospheric Chemistry and Physics*, *18*(3), 2097-2117, doi:10.5194/acp-18-2097-2018.

WMO (2014), Scientific Assessment of Ozone Depletion: 2014, Global Ozone Research and Monitoring Project*Rep.*, World Meteorological Organization, Geneva, Switzerland.

Zhang, Y., C. Li, N. A. Krotkov, J. Joiner, V. Fioletov, and C. McLinden (2017), Continuation of long-term global SO2 pollution monitoring from OMI to OMPS, *Atmospheric Measurement Techniques*, *10*(4), doi:10.5194/amt-10-1495-2017.

Ziemke, J. R., S. Chandra, B. N. Duncan, L. Froidevaux, P. K. Bhartia, P. F. Levelt, and J. W. Waters (2006), Tropospheric ozone determined from aura OMI and MLS: Evaluation of measurements and comparison with the Global Modeling Initiative's Chemical Transport Model, *Journal of Geophysical Research-Atmospheres*, *111*(D19), doi:10.1029/2006jd007089.

Ziemke, J. R., et al. (2019), Trends in global tropospheric ozone inferred from a composite record of TOMS/OMI/MLS/OMPS satellite measurements and the MERRA-2 GMI simulation, *Atmospheric Chemistry and Physics*, *19*(5), 3257-3269, doi:10.5194/acp-19-3257-2019.

Figure captions:

Figure 1: Annual mean anthropogenic emissions of (left) NOx, (middle) CO, and (right) VOCs (the sum of CH_2O, C_4H_8O, C_3H_6 and higher alkenes, C_2H_6, C_3H_8, C_4H_{10}, C_2H_4O) in the RefD1 simulation from 1960 to 2018 averaged over (Top) globe (90S-90N), NH (30N-90N), tropics (30S-30N) and SH (30S-90S). (Middle) anthropogenic emission regions including U.S., Europe, China, and India; (Bottom) Biomass burning regions including Africa, Indonesia, South America and Boreal regions.

Figure 2: Comparison of RefD1 against OMI tropospheric column ozone: the 2005-2018 averaged tropospheric column ozone (1-2pm local time) as a) derived from Aura OMI/MLS, b) simulated by GEOSCCM RefD1, c) the difference between simulations and observations. d) Right panel shows the observed (black) and simulated (red) global and hemispheric averaged tropospheric ozone column from 2005 to 2018. Dashed lines are corresponding linear least squares regression fits. Correlations, slopes ± 1.96*σ uncertainties, as well as relative changes of observed and simulated tropospheric column ozone are given in the inset. Y-axis ranges vary by region.

Figure 3: Similar as Figure 2, but for the comparison of RefD1 against OMI total column ozone.

Figure 4: The linear trends of Tropospheric column ozone (TCO) derived from top): Aura OMI/MLS measurements and bottom) GEOSCCM RefD1 simulation from 2005 to 2018. Numbers in the maps are the regional mean of TCO changes (in DU] calculated based on averaged

1115 trends during this period over four selected anthropogenic emission regions (US, Europe, India
1116 and China) and three selected biomass burning regions (South America, Africa and Indonesia).

1117 Figure 5: Temporal variations of simulated annual mean total column ozone (red dashed line) with
1118 the tropospheric column ozone stacked on top of the stratospheric column ozone from the RefD1
1119 simulation between 1960 and 2018, superimposed on the annual mean of total column ozone from
1120 ground-based observations (gray cross symbol) and merged satellite observations (black thick line)
1121 (Weber et al., 2018). A five-year low pass filter has been applied to the simulated ozone fields to
1122 highlight the long-term variations (red solid line).

1123 Figure 6: Temporal variations of observed (black) and simulated (red) ozone anomalies of (top)
1124 total ozone column, (middle) tropospheric column ozone and (bottom) stratospheric ozone column.
1125 Dashed lines are corresponding linear least squares regression fits. Slopes ± 1.96*σ uncertainties,
1126 absolute and relative changes of observations and simulations, as well as correlations are given in
1127 the inset.

1128 Figure 7: Changes in tropospheric column ozone (TCO, red) and stratospheric column ozone (blue)
1129 between 2005 and 2018 averaged over global, NH, tropics and SH, calculated from observations
1130 (bars with solid color) and RefD1 simulation (bars with patterned color).

1131 Figure 8: Comparison of RefD1 against OMI tropospheric column NO_2: Left Panel) the 2005-2018
1132 average tropospheric column NO_2 as derived from Aura OMI, simulated by GEOSCCM RefD1,
1133 and the difference between simulations and observations; Right panel) the observed (black) and
1134 simulated (red) global and hemispheric averaged tropospheric NO_2 column from 2005 to 2018.
1135 Dashed lines are corresponding linear least squares regression fits. Correlations, slopes ± 1.96*σ
1136 uncertainties, as well as relative changes of observed and simulated tropospheric column ozone
1137 are given in the inset. Y-axis ranges vary by region.

1138 Figure 9: Similar as Figure 8 but for the comparison of the RefD1 simulation against OMI total
1139 column CH_2O.

1140 Figure 10: Similar as Figure 8 but for the comparison of the RefD1 simulation against MOPITT
1141 total column CO.

1142 Figure 11: Time series of observed and simulated anomalies of TCO, $\Omega_{NO2,}$ $\Omega_{CH2O,}$ $\Omega_{CO,}$ as well as
1143 simulated tropospheric column of $StratO_3$ over four anthropogenic emission regions. Slopes ±
1144 1.96σ uncertainties, as well as relative changes of observations and simulations are given in the
1145 inset. Y-axis ranges vary by region.

1146 Figure 12: Regional trends in tropospheric column ozone and its key precursors (NO_2, CH_2O and
1147 CO) over the U.S. from 2005 to 2018 based on satellite observations including OMI/MLS TCO,
1148 OMI Ω_{NO2}, OMI Ω_{CH2O}, MOPITT Ω_{CO}; and simulations from the GEOSCCM RefD1.

1149 Figure 13: Similar as Figure 12 but for the comparison over Europe.

1150 Figure 14: Similar as Figure 12 but for the comparison over China.

1151 Figure 15: Time series of observed and simulated anomalies of TCO, $\Omega_{NO2,}$ $\Omega_{CH2O,}$ $\Omega_{CO,}$ as well as
1152 simulated tropospheric column of $StratO_3$ over three biomass burning emission regions. Slopes ±
1153 1.96σ uncertainties, as well as relative changes of observations and simulations are given in the
1154 inset. Y-axis ranges vary by region.

1155 Figure 16: Temporal time series of observed and simulated anomalies of TCO, Ω_{NO2}, Ω_{CH2O}, Ω_{CO},
1156 as well as simulated tropospheric column of $StratO_3$ over NH Ocean background region. Slopes ±
1157 1.96σ uncertainties, as well as relative changes of observations and simulations are given in the
1158 inset.

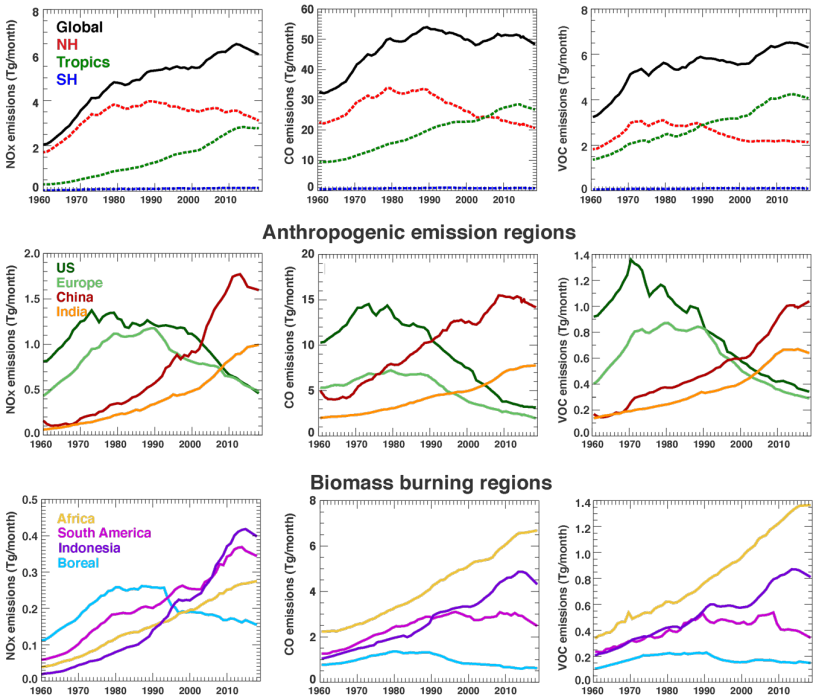

Figure 1: Annual mean anthropogenic emissions of (left) NOx, (middle) CO, and (right) VOCs (the sum of CH_2O, C_4H_8O, C_3H_6 and higher alkenes, C_2H_6, C_3H_8, C_4H_{10}, C_2H_4O) in the RefD1 simulation from 1960 to 2018 averaged over (Top) globe (90S-90N), NH (30N-90N), tropics (30S-30N) and SH (30S-90S). (Middle) anthropogenic emission regions including U.S., Europe, China, and India; (Bottom) Biomass burning regions including Africa, Indonesia, South America and Boreal regions.

1159

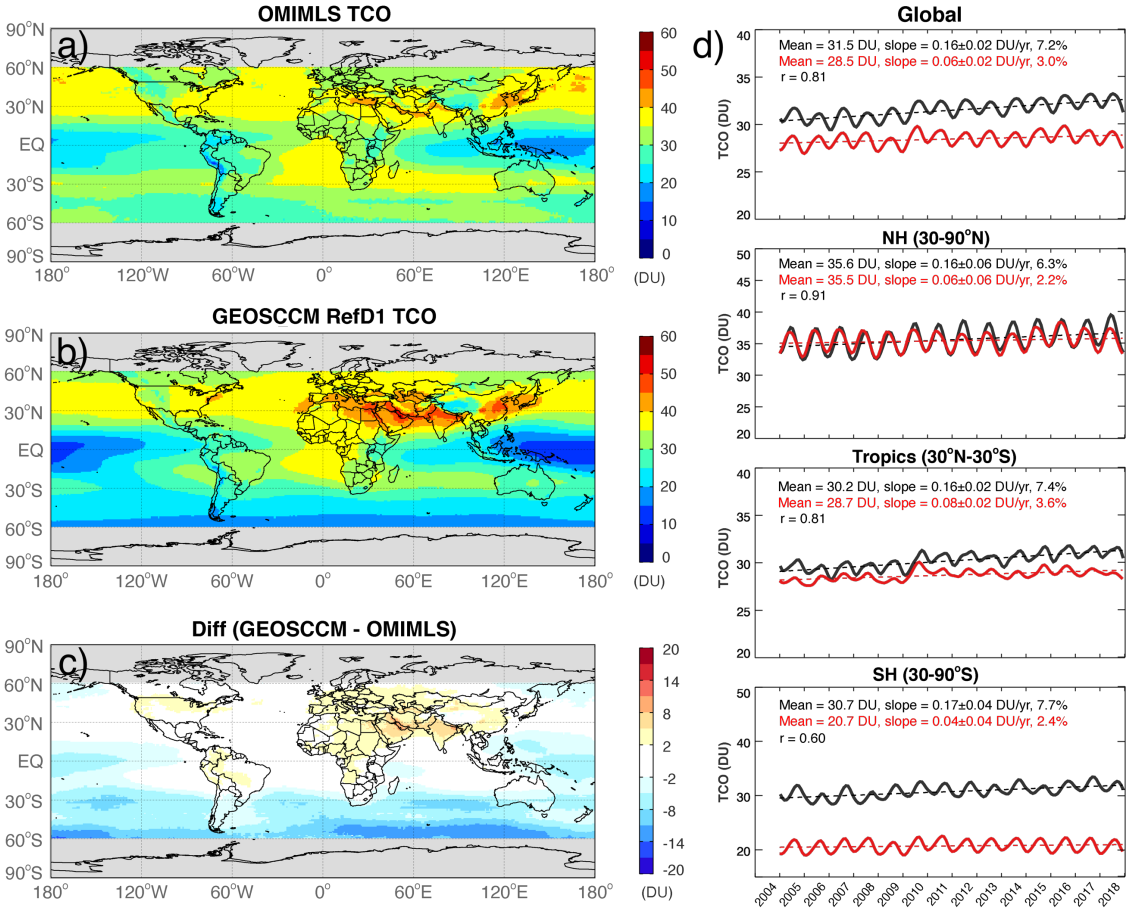

*Figure 2: Comparison of RefD1 against OMI tropospheric column ozone: the 2005-2018 averaged tropospheric column ozone (1-2pm local time) as a) derived from Aura OMI/MLS, b) simulated by GEOSCCM RefD1, c) the difference between simulations and observations. d) Right panel shows the observed (black) and simulated (red) global and hemispheric averaged tropospheric ozone column from 2005 to 2018. Dashed lines are corresponding linear least squares regression fits. Correlations, slopes ± 1.96*σ uncertainties, as well as relative changes of observed and simulated tropospheric column ozone are given in the inset. Y-axis ranges vary by region.*

1160

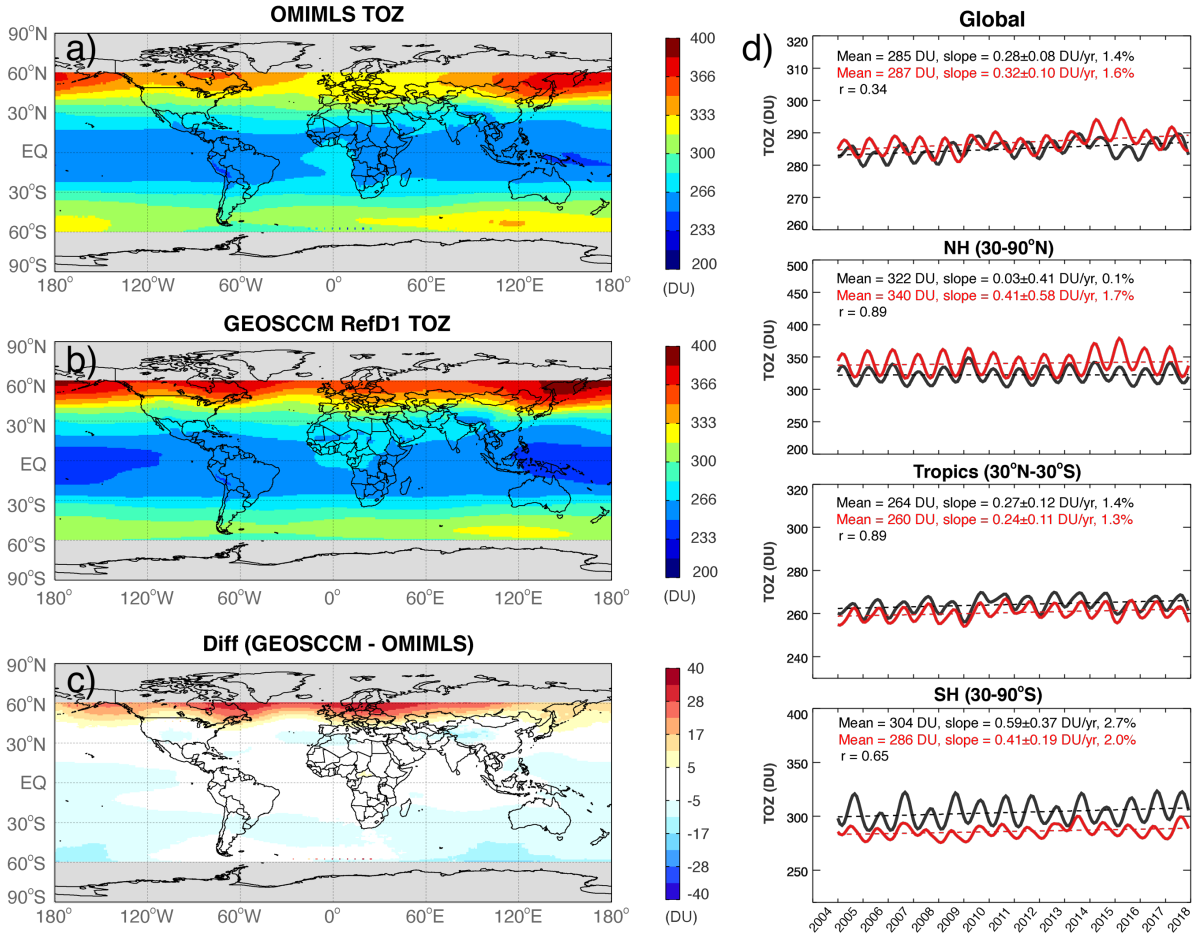

Figure 3: Similar as Figure 2, but for the comparison of RefD1 against OMI total column ozone.

1161

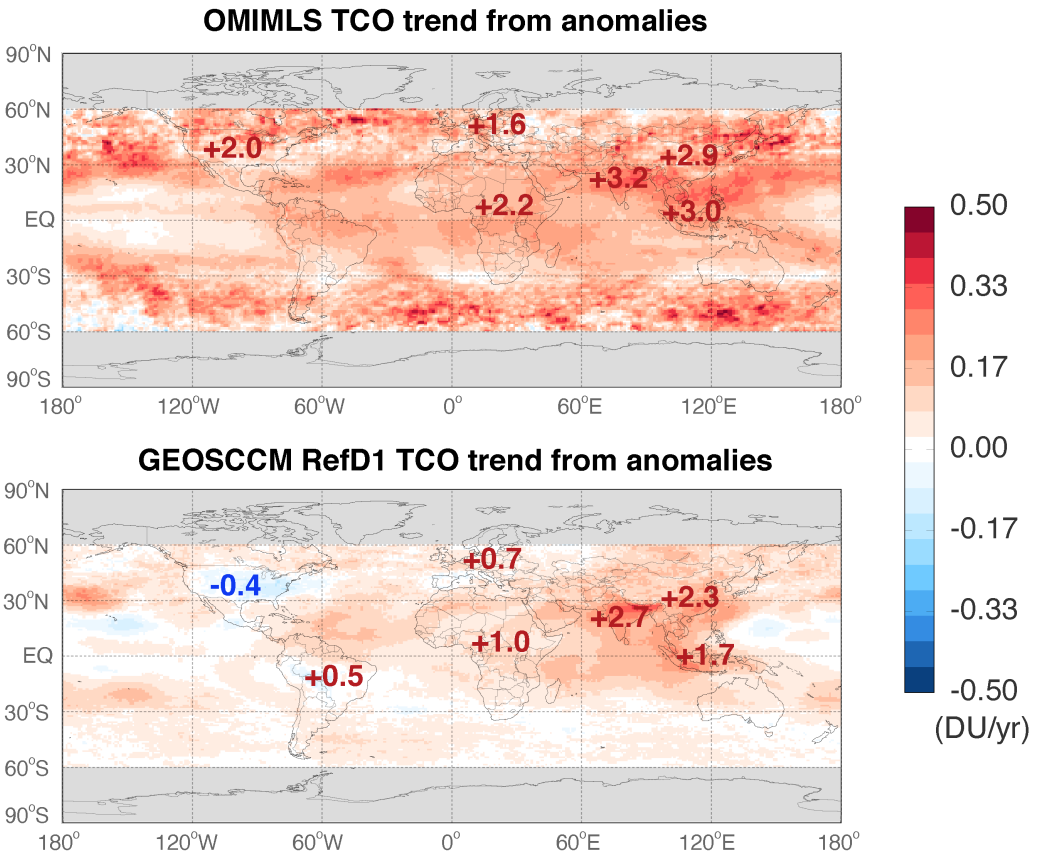

Figure 4: The linear trends of Tropospheric column ozone (TCO) derived from top): Aura OMI/MLS measurements and bottom) GEOSCCM RefD1 simulation from 2005 to 2018. Numbers in the maps are the regional mean of TCO changes (in DU] calculated based on averaged trends during this period over four selected anthropogenic emission regions (US, Europe, India and China) and three selected biomass burning regions (South America, Africa and Indonesia).

1162

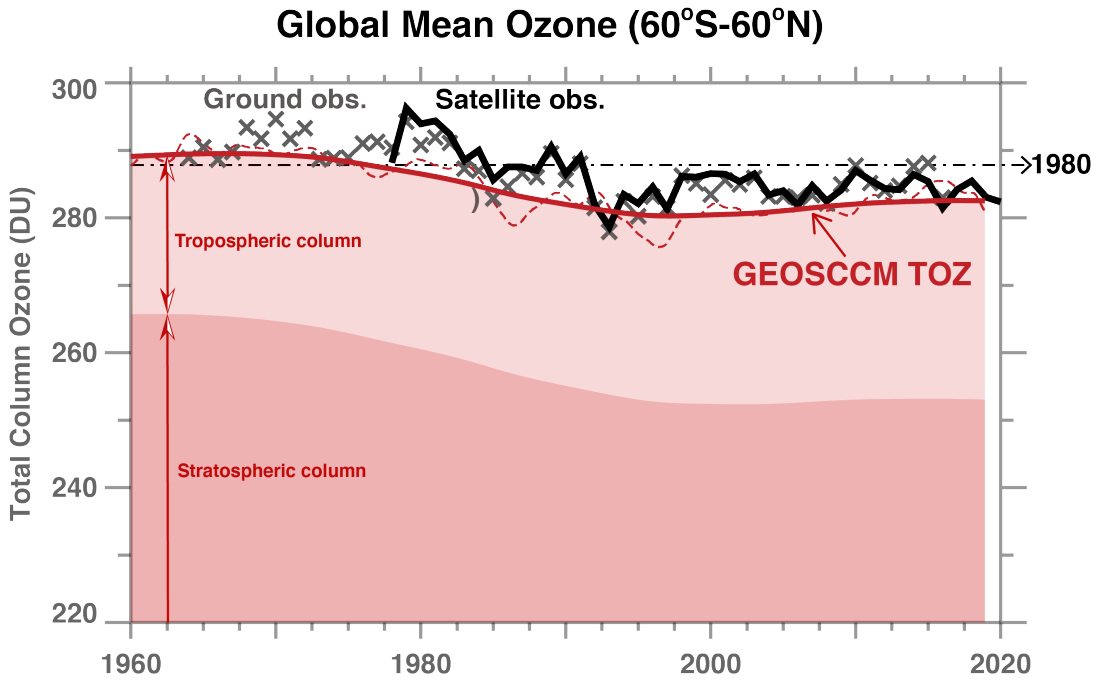

Figure 5: Temporal variations of simulated annual mean total column ozone (red dashed line) with the tropospheric column ozone stacked on top of the stratospheric column ozone from the RefD1 simulation between 1960 and 2018, superimposed on the annual mean of total column ozone from ground-based observations (gray cross symbol) and merged satellite observations (black thick line) (Weber et al., 2018). A five-year low pass filter has been applied to the simulated ozone fields to highlight the long-term variations (red solid line).

1163

1164

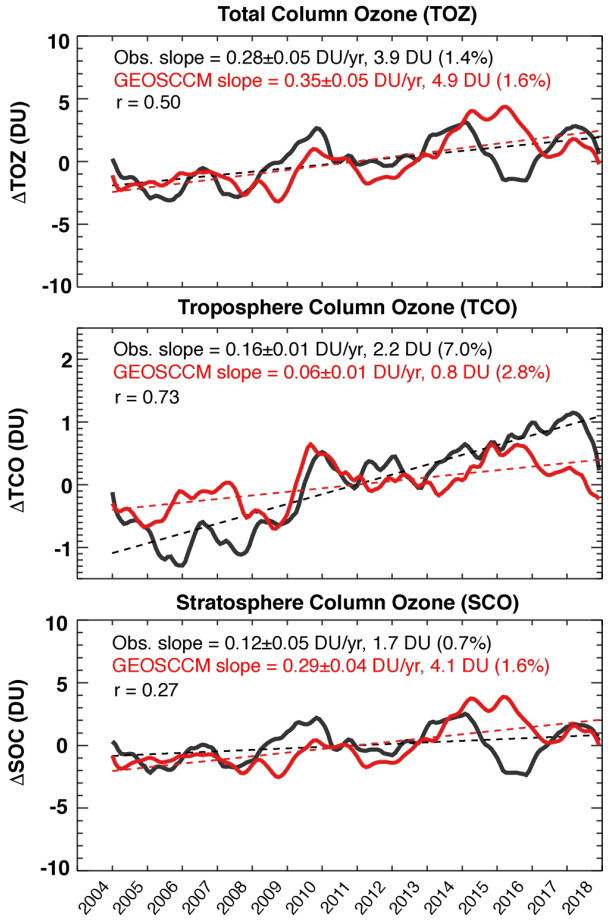

*Figure 6: Temporal variations of observed (black) and simulated (red) ozone anomalies of (top) total ozone column, (middle) tropospheric column ozone and (bottom) stratospheric ozone column. Dashed lines are corresponding linear least squares regression fits. Slopes ± 1.96*σ uncertainties, absolute and relative changes of observations and simulations, as well as*

1165

1166

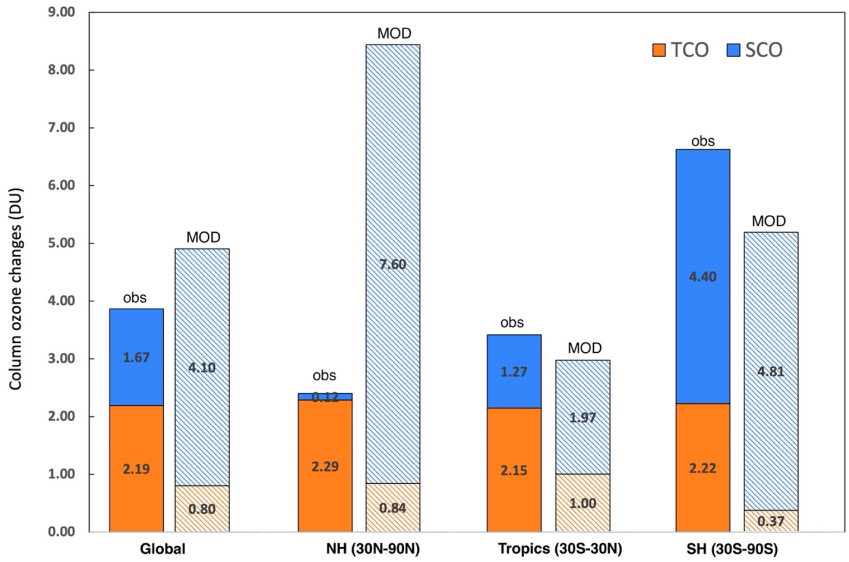

Figure 7: Changes in tropospheric column ozone (TCO, red) and stratospheric column ozone (blue) between 2005 and 2018 averaged over global, NH, tropics and SH, calculated from observations (bars with solid color) and RefD1 simulation (bars with patterned color).

1167

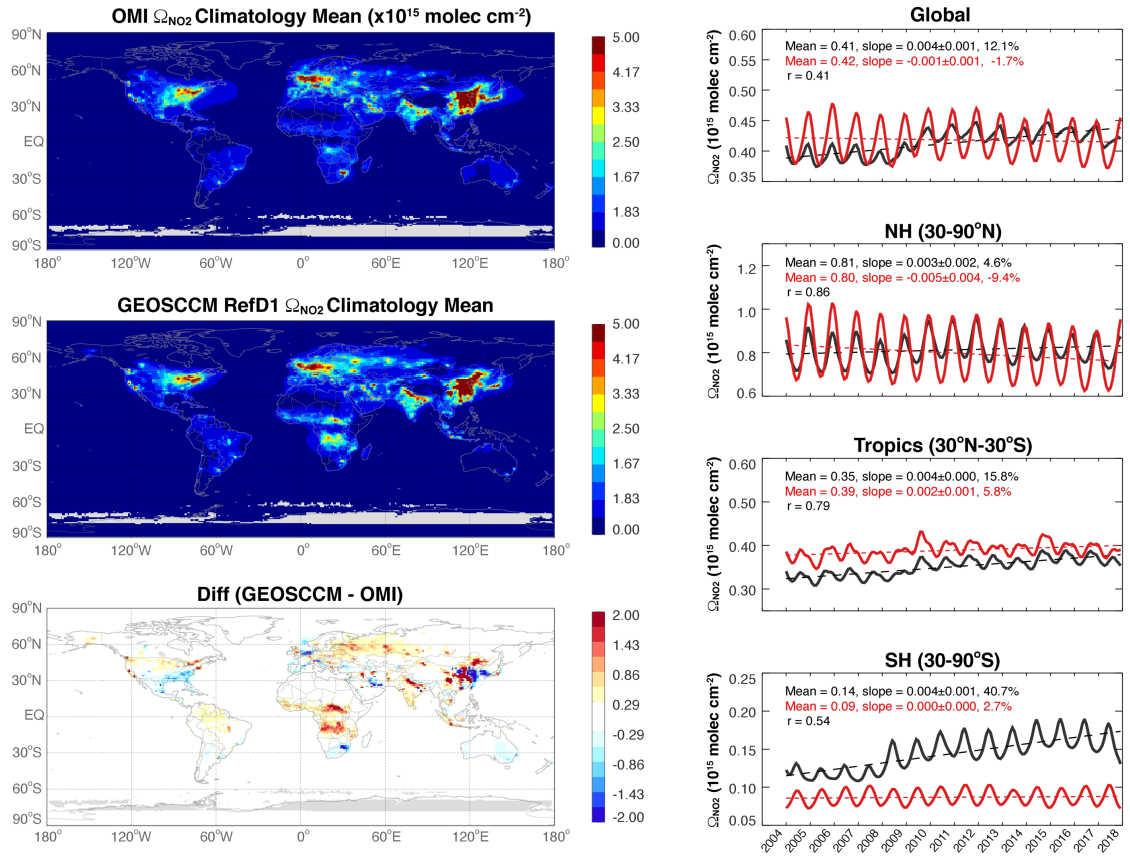

*Figure 8: Comparison of RefD1 against OMI tropospheric column NO_2: Left Panel) the 2005-2018 average tropospheric column NO_2 as derived from Aura OMI, simulated by GEOSCCM RefD1, and the difference between simulations and observations; Right panel) the observed (black) and simulated (red) global and hemispheric averaged tropospheric NO_2 column from 2005 to 2018. Dashed lines are corresponding linear least squares regression fits. Correlations, slopes ± 1.96*σ uncertainties, as well as relative changes of observed and simulated tropospheric column ozone are given in the inset. Y-axis ranges vary by region.*

1168

1169

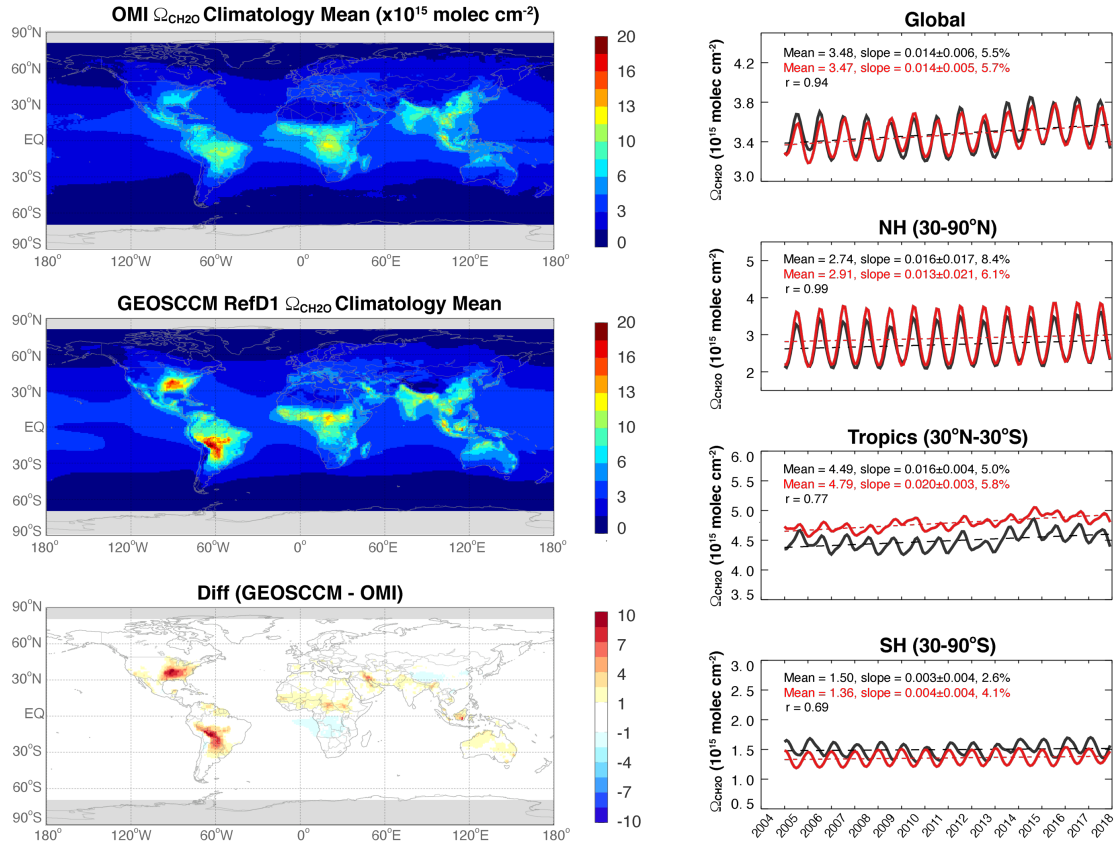

Figure 9: Similar as Figure 8 but for the comparison of the RefD1 simulation against OMI total column CH_2O.

1170

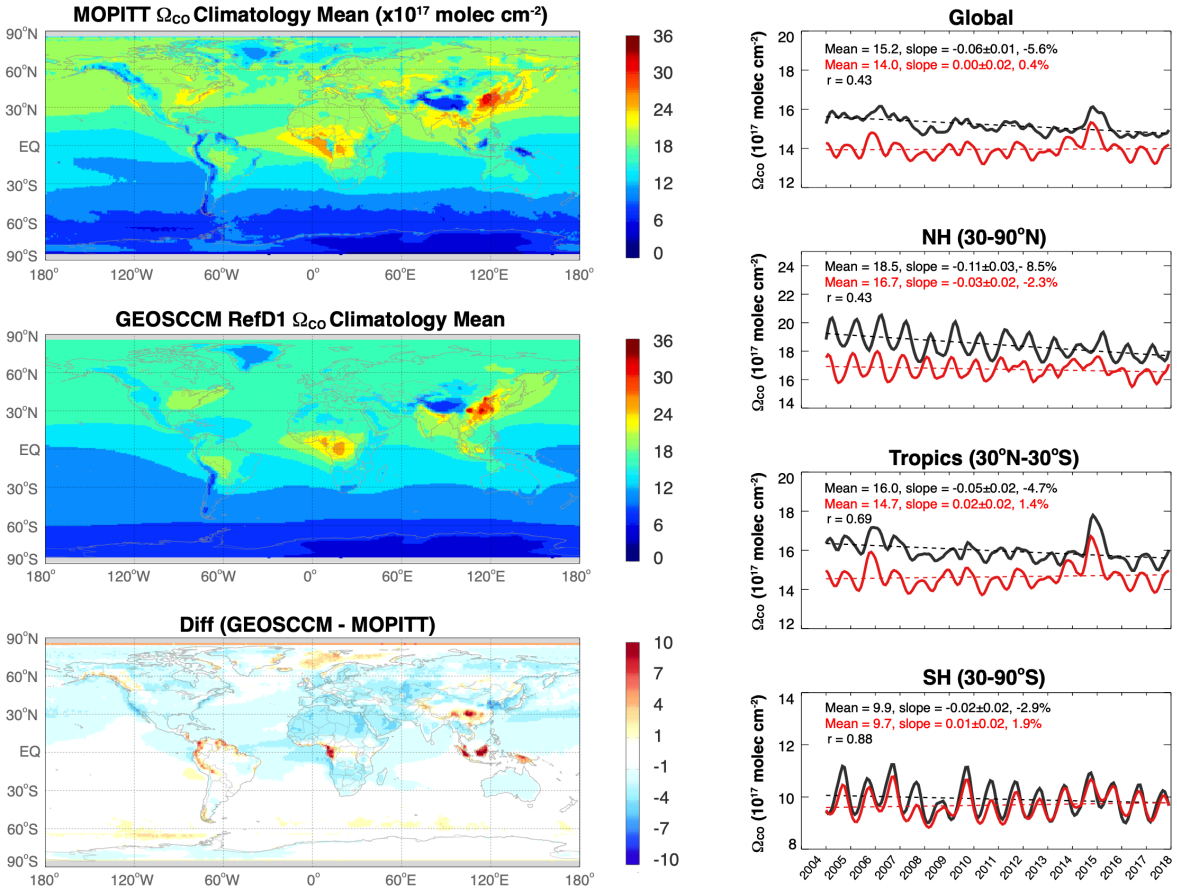

Figure 10: Similar as Figure 8 but for the comparison of the RefD1 simulation against MOPITT total column CO.

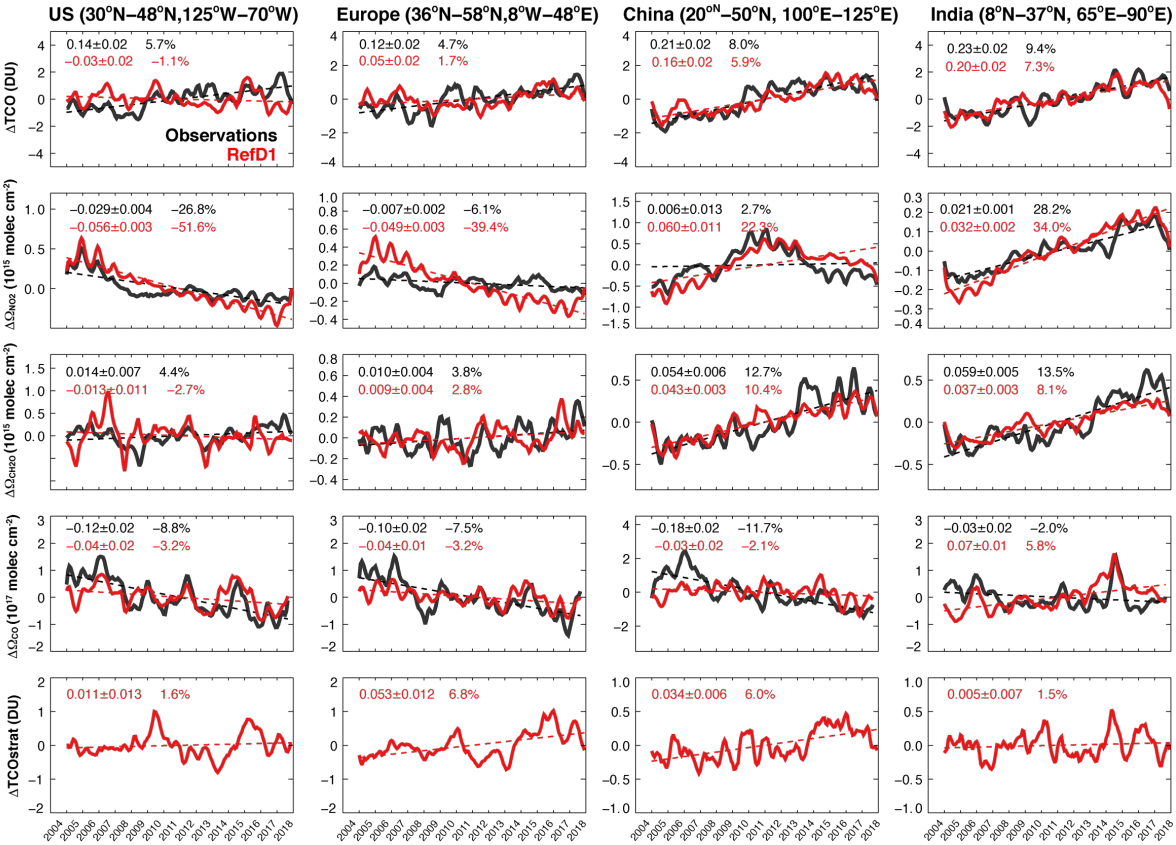

Figure 11: Time series of observed and simulated anomalies of TCO, Ω_{NO2}, Ω_{CH2O}, Ω_{CO}, as well as simulated tropospheric column of StratO_3 over four anthropogenic emission regions. Slopes ± 1.96σ uncertainties, as well as relative changes of observations and simulations are given in the inset. Y-axis ranges vary by region.

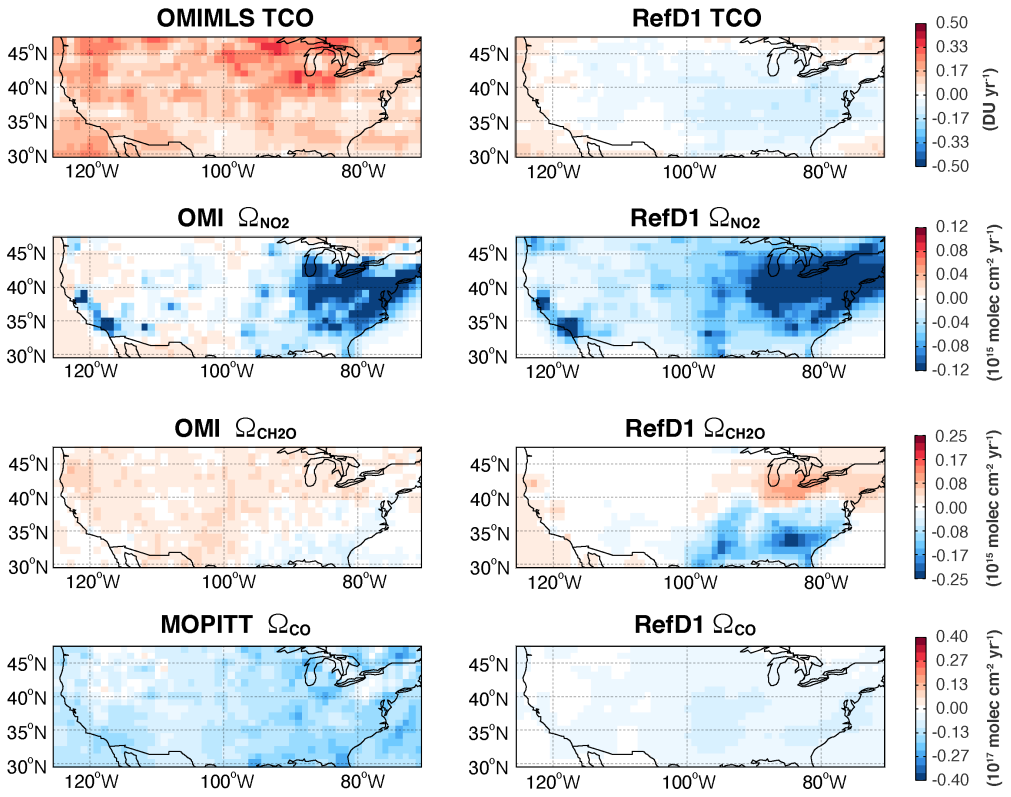

Figure 12: Regional trends in tropospheric column ozone and its key precursors (NO_2, CH_2O and CO) over the U.S. from 2005 to 2018 based on satellite observations including OMI/MLS TCO, OMI Ω_{NO2}, OMI Ω_{CH2O}, MOPITT Ω_{CO}; and simulations from the GEOSCCM RefD1.

1175

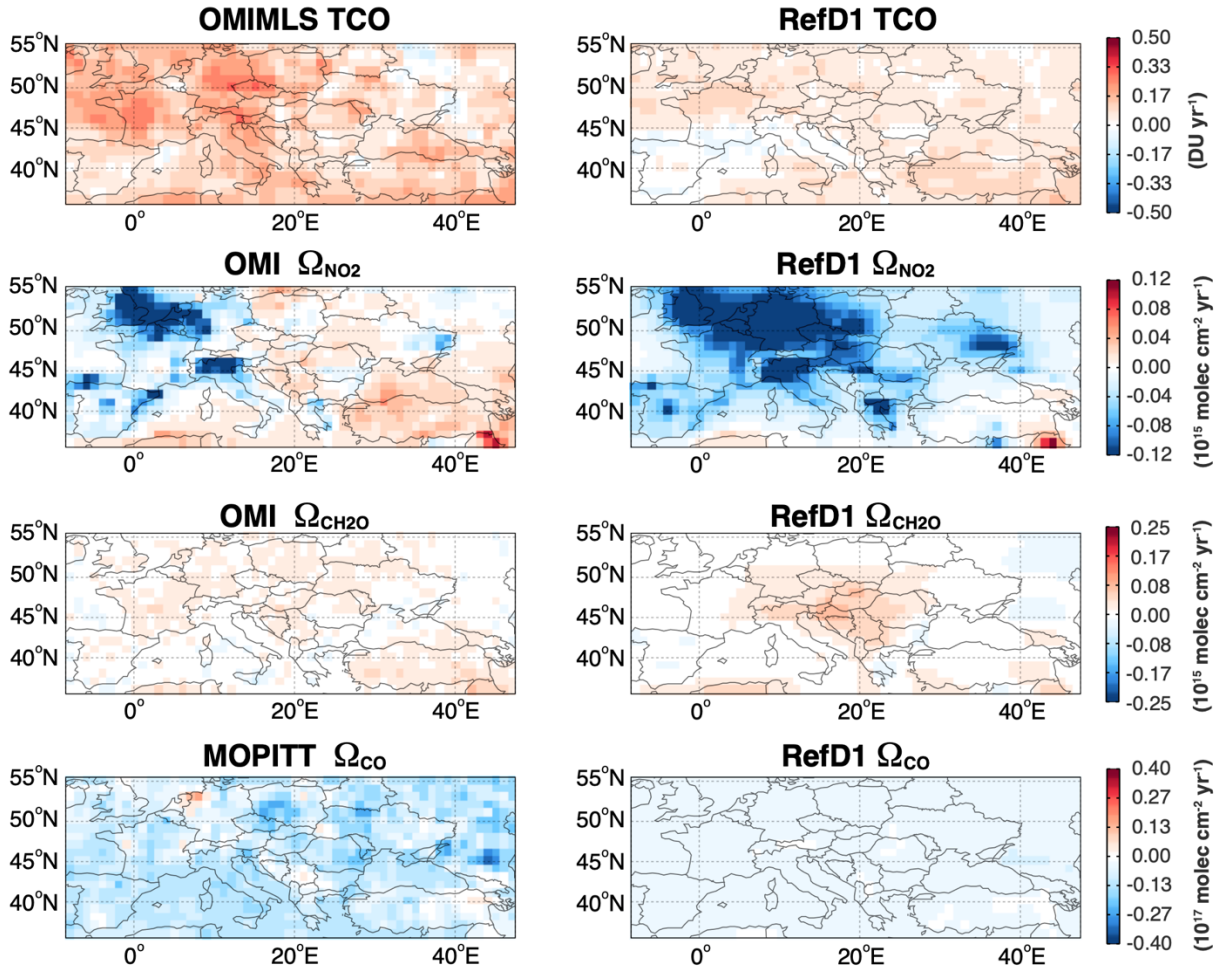

Figure 13: Regional trends in tropospheric column ozone and its key precursors (NO_2, CH_2O and CO) over the Europe from 2005 to 2018 based on satellite observations including OMI/MLS TCO, OMI Ω_{NO2}, OMI Ω_{CH2O}, MOPITT Ω_{CO}; and simulations from the GEOSCCM RefD1.

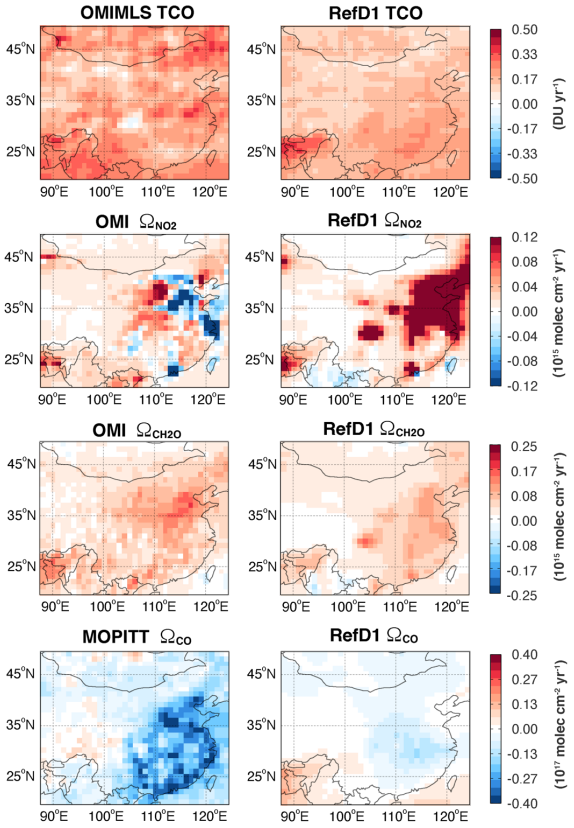

Figure 14: Similar as Figure 12 but for the comparison over China.

1180

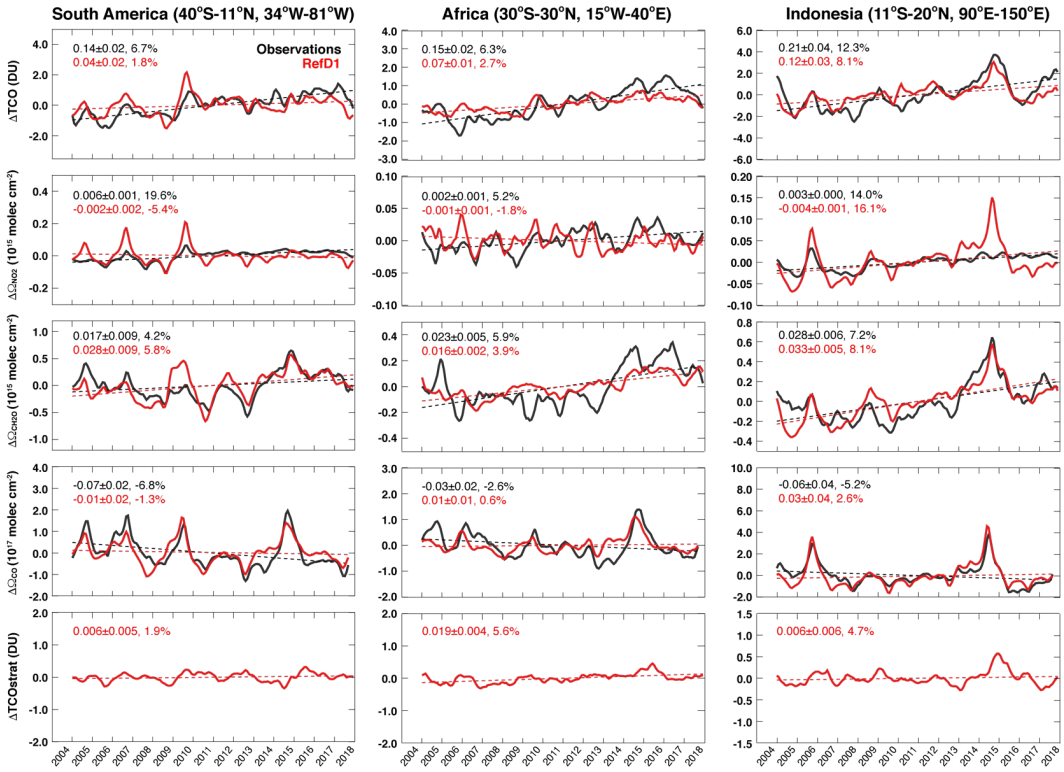

Figure 15: Time series of observed and simulated anomalies of TCO, Ω_{NO2}, Ω_{CH2O}, Ω_{CO}, as well as simulated tropospheric column of $StratO_3$ over three biomass burning emission regions. Slopes ± 1.96σ uncertainties, as well as relative changes of observations and simulations are given in the inset. Y-axis ranges vary by region.

1181

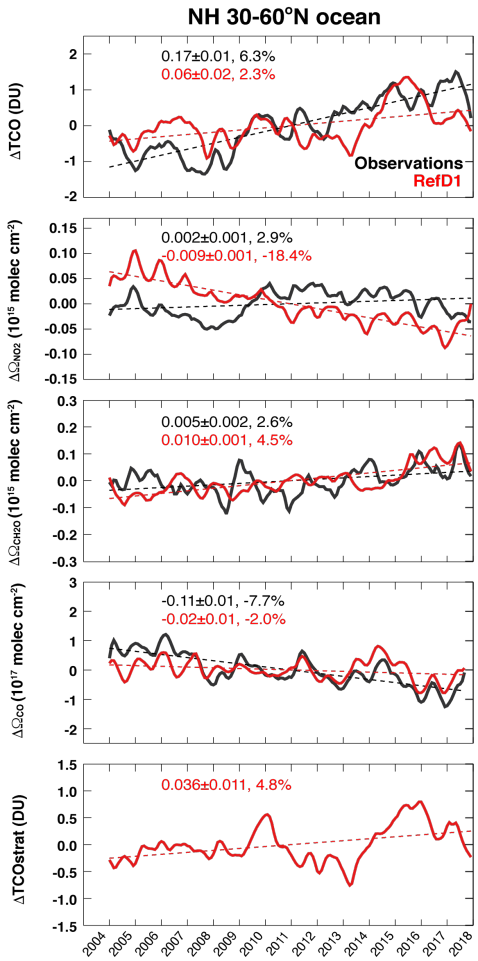

Figure 16: Temporal time series of observed and simulated anomalies of TCO, Ω_{NO2}, Ω_{CH2O}, Ω_{CO}, as well as simulated tropospheric column of StratO_3 over NH Ocean background region. Slopes ± 1.96σ uncertainties, as well as relative changes of observations and simulations are given in the inset.

1182

1183